UNIVERSITÉ DE SHERBROOKE
Faculté de génie
Département de génie mécanique

DÉVELOPPEMENT D'UN DRONE PERCHEUR POUR ATTERRISSAGE ET GRIMPE SUR DES SURFACES VERTICALES

Mémoire de maitrise
Spécialité : génie mécanique

Dino MEHANOVIĆ

Sherbrooke (Québec) Canada

Juin 2018

MEMBRES DU JURY

Alexis LUSSIER DESBIENS

Directeur

David RANCOURT

Évaluateur

Mathieu PICARD

Évaluateur

RÉSUMÉ

Ce projet visait le développement du premier drone à aile fixe capable de se percher de façon autonome sur des surfaces verticales et d'en décoller. Inspiré par les oiseaux, l'avion développé utilise une manoeuvre de cabrage assistée par la poussée pour rapidement ralentir avant de se poser. Des microgriffes sont utilisées pour permettre à l'avion de s'accrocher à des surfaces rugueuses, alors que le contrôle de la manoeuvre est entièrement embarqué. L'effet de la poussée aérodynamique sur l'enveloppe d'atterrissage de l'avion est analysée et un contrôleur de vitesse verticale est proposé pour créer des descentes fluides et robustes vers un mur. Plusieurs atterissages ont été testé, à travers une plage de conditions de vol. La poussée aérodynamique de l'avion est également utilisée pour grimper le long de surfaces verticales. Des modèles aérodynamiques sont utilisés pour prédire les performance de l'avion dans plusieurs régimes de grimpe aérienne, et sélectionner un contrôleur pour le maintien d'une distance fixe avec un mur en montée verticale. La manoeuvre de grimpe est testée à l'intérieur et à l'extérieur, pour des grimpes courtes et longues.

Mots-clés : Drone percheur, Atterrissage vertical, Grimpe aérienne

TABLE DES MATIÈRES

LISTE DES FIGURES

LISTE DES TABLEAUX

CHAPITRE 1

INTRODUCTION

1.1 Mise en contexte et problématique

Les applications civiles des véhicules aériens autonomes (UAV) sont de plus en plus nombreuses et diversifiées. Par exemple, des compagnies utilisent présentement des véhicules multi-rotors pour voler à proximité de bâtiments, afin de prélever des images utiles à l'inspection de leur structure. L'usage de drones pour cette application vise à éviter l'exposition d'êtres humains à des situations possiblement dangereuses, comme le travail en hauteur.

De façon similaire, des drones pourraient être utilisés par des équipes de sismologues, afin d'éviter l'exposition à des situations dangereuses au moment de sonder des zones touchées par des séismes. Le prélèvement de telles données est problématique en raison de la difficulté d'accès des lieux en ruines et la possibilité de secousses sismiques supplémentaires. De plus, ce type de catastrophe naturelle peut mener à la destruction des réseaux de communications en place. L'envoi de groupes de drones permettrait donc d'établir temporairement des réseaux de communications mobiles, pour accélérer les différentes opérations de sauvetage et de reconstruction dans les zones sinistrées.

Ainsi, que ce soit pour établir des réseaux de communication stables sur de longues périodes, ou réaliser toutes autres tâches nécessitant de s'immobiliser, les drones doivent être capables d'atterrir. Pour plusieurs applications, cela implique d'être en mesure de se percher sur des surfaces verticales (ex. : prises d'images à proximité de structures). Dans le cas de zones ayant subi des tremblements de terre, il est compliqué de se poser au sol en raison des ruines, mais des structures verticales partiellement détruites demeurent en place.

Présentement, plusieurs robots grimpeurs sont capables d'interagir avec ces surfaces verticales, mais ils ne sont pas pleinement autonomes. Ils doivent être positionnés et/ou retirés par des humains. Les drones capables d'atterrir sur des surfaces verticales, et d'en décoller, sont quant à eux peu nombreux. Notamment aucun UAV à aile fixe n'est capable de réaliser ces deux tâches, primordiales pour être pleinement autonome. Leur surface alaire présente toutefois un net avantage par rapport aux quadrotors, car elle permet d'intégrer efficacement des technologies de recharge solaire, ouvrant la porte à des missions de durées

indéfinies. De plus, cette surface alaire réduit la consommation d'énergie lors de longs vols (meilleurs ratio portance/traînée).

Le défi principal dans le développement de ce type de plateforme est la nécessité d'avoir un niveau d'autonomie élevé, pour garantir des atterrissages réussis sous différentes conditions de vol. Ainsi, en plus de nécessiter un mécanisme d'atterrissage suffisamment robuste, les atterrissages requièrent le développement de contrôleurs fiables. Puis, pour permettre à une plateforme aérienne de se déplacer sur des surfaces verticales, de nombreux choix de conception se présentent. Par exemple, un drone pourrait utiliser des pattes actionnées pour grimper, ou il pourrait encore utiliser la poussée de son hélice, en effectuant un vol vertical ou une trajectoire avec une vitesse horizontale.

1.2 Définition du projet de recherche

Le développement de drones et de robots toujours plus performants a récemment mené à des plateformes intégrant plusieurs modes d'opérations (ex. : vol et grimpe de surfaces verticales). Ce nouveau type de robots multimodals ouvre la porte à des applications uniques, mais demande aussi de considérer différemment la conception d'une plateforme robotisée. Alors que les robots grimpeurs sont efficaces pour naviguer le long de surfaces verticales, ils demeurent peu autonomes et peuvent difficilement transiter vers des déplacements au sol. De l'autre côté, les plateformes aériennes capable de se percher sur des murs sont plus versatiles, mais elles sont soit incapables de décoller des surfaces verticales (avions), soit peu efficaces dans leurs transitions entre leur mode perché et leur mode de déplacement aérien (quadrotors). L'intégration directe des capacités d'un robot grimpeur et d'un robot aérien dans une plateforme unique impose également certains problèmes d'efficacité, puisqu'une partie de la masse totale du système n'est pas utilisée dans chacun des deux modes d'opération.

Ce projet vise donc à développer un drone multimodal, capable d'utiliser efficacement un système de propulsion unique pour le vol et pour la grimpe de surfaces verticales.

1.3 Objectifs du projet de recherche

À la lumière des observations précédentes, l'objectif principal du projet est le suivant :

Développer un drone à aile fixe capable d'atterrir et grimper sur des surfaces verticales

De cet objectif global découle une série d'objectifs secondaires :

1. Intégrer un mécanisme d'atterrissage à microgriffes sur un avion miniature
2. Développer un modèle prédictif de l'impact avec le mur pour déterminer les conditions permettant de réussir un atterrissage
3. Concevoir un contrôleur pour la manoeuvre motorisée de transition du vol horizontal à l'atterrissage sur le mur
4. Implémenter une logique de contrôle pour les déplacements sur les murs et les décollages

L'atteinte de ces objectifs secondaires assurera la réussite du projet.

1.4 Contributions originales

Ce projet propose quatre contributions originales distinctes.

- Un nouveau drone percheur capable d'atterrir et de grimper de façon autonome sur des surfaces verticales
- Un simulateur permettant de prédire la réussite ou l'échec de tentatives d'atterrissage
- Une nouvelle stratégie de contrôle pour des manoeuvres d'atterrissages de drones percheurs
- Des principes de conception de robots multimodals

1.5 Plan du document

Ce document se divise en trois parties. La section 2 présente une analyse des robots grimpeurs et des drones percheurs existants. La section 3 présente un article publié, expliquant le processus de développement et d'analyse d'un drone percheur, capable d'exécuter des atterrissages et des décollages verticaux assistés par la poussée aérodynamique. Enfin, la section 4 présente un article soumis pour publication, détaillant l'analyse et l'implémentation de la grimpe aérienne de surfaces verticales avec un drone à voilure fixe.

CHAPITRE 2

ÉTAT DE L'ART

2.1 Robots grimpeurs et robots multimodals

Les robots actuels sont généralement conçus pour des tâches précises ou des modes d'opération uniques. Certaines de ces plateformes se trouvent toutefois à avoir une habileté peu commune : grimper sur des surfaces verticales [11]. Un robot comme le Klingon peut même se percher sur un mur suite à une trajectoire balistique (Fig. 2.1 [5]).

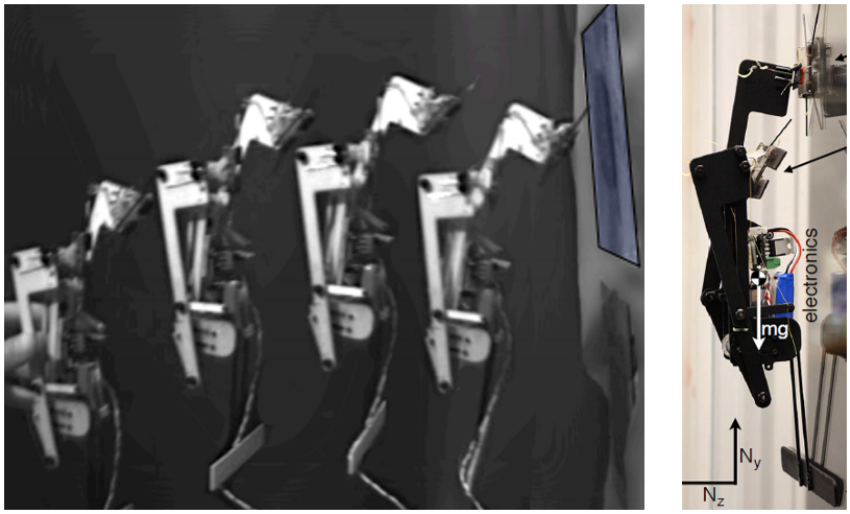

Figure 2.1 Le robot grimpeur Klingon capable de se percher sur des murs.

Ces capacités peu typiques des robots grimpeurs leurs permettent donc d'être versatiles dans leurs déplacements, mais ils demeurent peu autonomes (nécessitent un facteur humain pour transiter entre différents modes d'opération). Ils doivent généralement être lancés ou positionnés sur un mur, puis retirés par un humain pour débuter ou terminer leurs missions [5, 11, 21, 35]. Par contre, plusieurs UAV sont en mesure de se percher sur des surfaces verticales sans intervention humaine quelconque. Cette habileté, en plus d'ouvrir la porte à des applications uniques, est un requis pour la réalisation de missions de longues durées par des UAV miniatures. En effet, l'utilisation de la recharge solaire n'est présentement pas assez efficace pour permettre à un drone de petite taille de demeurer continuellement en vol [31]. Cela contraint les drones à demeurer au repos durant des parties d'une mission, pour la recharge de leurs batteries.

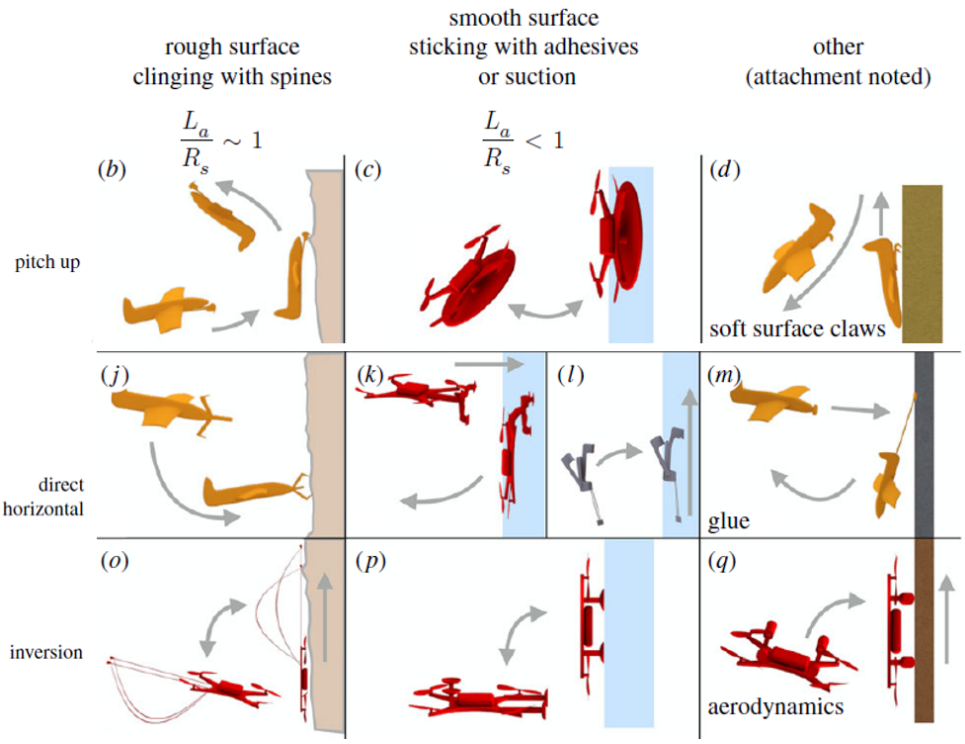

Figure 2.2 Revue des stratégies d'atterrissage sur des surfaces verticales [38].

Ainsi, ces drones utilisent des stratégies variées (Fig. 2.2) pour atterrir sur différents types de surfaces, tel que passé en revue par Roderick et al. [38]. La majorité de ces plateformes sont des quadrotors, tel que le SCAMP (Fig. 2.3 [33]), des plateformes n'offrant pas la possibilité d'intégrer efficacement des panneaux solaires. pour la recharge des batteries

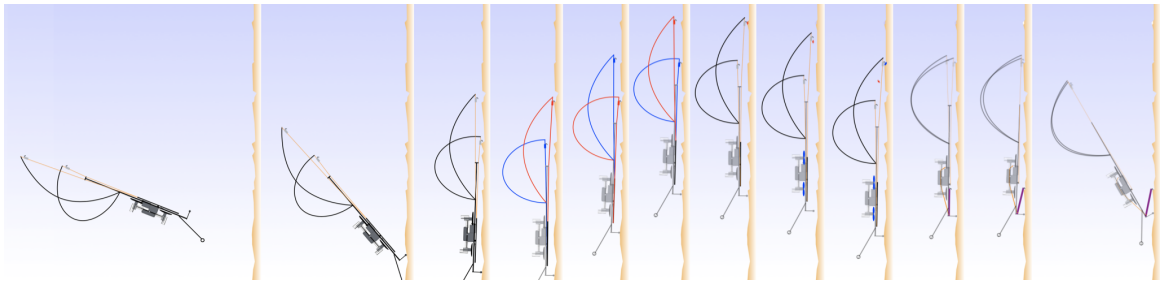

Figure 2.3 Le manoeuvre d'atterrissage et la technique de grimpe du quadorotor multimodal SCAMP [33].

Il est également montré dans cette revue des techniques de perchage que des planeurs sont capables d'atterrir en utilisant des méthodes distinctes : manoeuvre de cabrage [20], approche directe [16], etc.

Par contre, on remarque qu'il n'existe pas de drone à aile-fixe motorisé capable de se percher. L'absence de motorisation sur ces planeurs limite grandement leur application dans

des situations réelles. Toutefois, en faisant atterrir un avion motorisé avec un manoeuvre de cabrage, il devient simple de décoller et potentiellement efficace d'utiliser la poussée aérodynamique pour grimper le long d'un mur (Fig. 2.4).

Figure 2.4 Un drone à aile-fixe capable de décoller de surface verticales [20].

La recherche actuelle a donc pour but de se baser sur les travaux précédents ayant permis à un planeur miniature d'atterrir sur des murs, à l'aide d'une manoeuvre de cabrage [20]. La masse élevée de l'électronique (capteur de distance de 90 g) était l'un des défis principaux identifiés lors du développement de ces avions. La technologie actuelle (capteurs de moins de 20 g) permet donc d'outrepasser ce défi d'envergure. Entre autres, la logique de contrôle pour un atterrissage motorisé peut être adressée avec plus une grande attention.

À noter que le seul véhicule capable d'interagir pleinement avec les surfaces verticales (atterrir, grimper, décoller) est le SCAMP [33]. Le SCAMP utilise un mécanisme à deux servomoteurs pour actionner deux pattes munies de microgriffes [1]. Il réalise ainsi une démarche articulée pour se déplacer. La stratégie visée par ce projet est l'usage de la poussée du moteur pour se propulser vers le haut, de façon à sautiller sur le mur. L'orientation avantageuse du moteur, en position perchée, permet cette approche qui minimise la quantité de systèmes indépendants.

2.2 Adhésion

Les technologies d'adhésion diffèrent selon le type de surface visée. En effet, il y a une grande diversité topologique à travers les différentes surfaces naturelles et artificielles disponibles pour des atterrissages. Les applications visées par ce projet demandent d'interagir

avec des structures telles que des bâtiments, donc l'adhésion à des surfaces naturelles n'est pas considérée. Le tableau suivant fait état de quatre technologies d'adhésion en plein essor dans le domaine des robots grimpeurs et des drones percheurs.

Tableau 2.1 Technologies d'adhésion et caractéristiques générales

Technologie d'adhésion	**Surface d'adhésion**	**Principe d'adhésion**
Adhésifs Gecko	Lisse	Forces de Van der Waals
Électroadhésion (EA)	Lisse, ± ruguese	Force électrostatique
Hybrides Gecko/EA	Lisse	Électrostatique/Van der Waals
Microgriffes	Rugueuse	Blocage mécanique, friction

D'abord, les adhésifs de type Gecko [5, 32] présentent encore un manque de robustesse pour les applications en environnement non-contrôlé. Effectivement, ces surfaces s'usent particulièrement vite lorsque des essais d'adhésion sont faits sur des surfaces trop rugueuses. Or, la topologie d'une surface ne peut pas toujours être prédite avant une tentative d'atterrissage.

Une technologie comme l'électroadhésion[34] permet quant à elle d'interagir de façon robuste avec une gamme de surfaces plus variée, en raison d'une fragilité moindre. En effet, contrairement aux adhésifs Gecko, l'efficacité de l'électroadhésion ne repose pas sur la tenue de structures de l'ordre du micromètre. Cette technologie pourrait donc être prometteuse pour l'application visée, mais les forces en jeu à l'impact avec un mur peuvent être trop élevées pour garantir l'adhésion. Pour y remédier, les travaux de Kalantari et al. [13] sur un quadrotor percheur ont fait usage d'un mécanisme hybride, combinant l'électroadhésion et les surfaces de type Gecko pour étendre la plage de forces permissibles. Toutefois, la gamme de surfaces propices à l'adhésion, de même que la robustesse et la durabilité du mécanisme sont diminuées par la présence d'adhésifs de type Gecko.

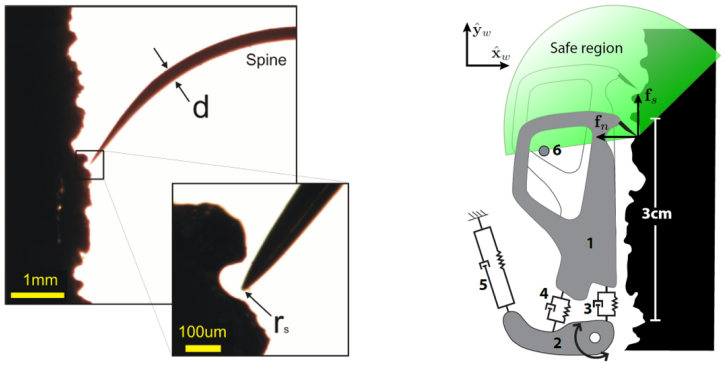

Figure 2.5 Vue détaillée d'une microgriffe qui s'engage dans les aspérités d'une surface rugueuse typique [1] (gauche) et représentation schématique d'une microgriffe insérée dans des aspérités, avec la zone accepable de forces tangentielles et normales [20] (droite).

Parmi les technologies d'adhésion à l'étude, les microgriffes présentent le plus de robustesse pour des tentatives d'adhésion à des surfaces pour lesquelles elles ne sont pas conçues. Par exemple, des adhésifs inspirés du Gecko peuvent être abîmés au contact de surfaces trop rugueuses, alors que les microgriffes ne sont pas altérées au contact de surfaces trop lisses. Ces microgriffes sont en fait des mécanismes 2D, en mouvement dans un seul plan (Fig. 2.5). Des hameçons sont utilisés à l'extrémité du mécanisme pour adhérer aux surfaces. En effet, les hameçons ont un rayon assez fin pour s'insérer dans les aspérités de surfaces rugueuses (brique, stucco, bardeau d'asphalte, etc.). Ces aspérités bloquent mécaniquement l'hameçon, alors que la surface exerce également une force de friction. Toutefois, des charges trop élevées sur ces fines aspérités peuvent les briser et mener à des échecs d'adhésion catastrophiques.

Ainsi, les microgriffes comportent une portion flexible dans leur structure (Fig. 2.6) et sont généralement utilisées en groupes. Cela permet de se conformer à la surface non-uniforme, pour distribuer sur plusieurs aspérités la charge totale à supporter (Fig. 2.6).

Figure 2.6 Microgriffes individuelle (gauche) et assemblage de microgriffes (droite).

De plus, les microgriffes sont des mécanismes directionnels. En effet, elles peuvent être analysées à travers les composantes de force normales et tangentielles de la force de réaction qu'elles subissent, pour déterminer s'il y a adhésion ou pas (Fig. 2.5). Afin d'analyser les atterrissages, un modèle dynamique d'impact avec le mur pourrait donc être développé. En combinaison avec les critères sur les forces tangentielles et normales, ce modèle permettrait de prédire la plage de vitesses d'impact permissibles pour réussir à se percher. Ultimement, ce modèle pourrait être utilisé comme outil d'optimisation de la suspension [20].

2.3 Contrôle

La plateforme visée par ce projet étant un drone autonome dans un environnement extérieur, tout le contrôle et la détection se doivent d'être embarqués. Afin de cibler une approche répondant à ces critères, une étude de différents contrôleurs pour drones à ailes

fixes est réalisée. Plus particulièrement, l'étude fait une courte revue des contrôleurs utilisés pour réaliser des manoeuvres agiles.

D'abord, afin de permettre à un planeur d'atterrir sur un fil, une stratégie de contrôle avancée, faisant usage de LQR-Trees (Linear Quadratic Regulator), a été appliquée avec succès [26]. Par contre, cette approche de contrôle requiert à la fois une grande puissance de calcul et un système de capture de mouvement non-embarqué permettant de connaître précisément la position du véhicule.

D'autres avancées récentes en contrôle ont permis à de petits avions motorisés de transiter vers un vol stationnaire vertical, à partir d'une large gamme de conditions initiales [37]. Ces travaux réussissent ainsi à combiner la manoeuvrabilité des véhicules aériens multi-rotors avec la rapidité et l'endurance des plateformes à aile-fixe. Toutefois, les algorithmes développés nécessitent un système de capture de mouvement non-embarqué, tout comme les travaux mentionnés au paragaphe précédent.

Les travaux sur l'atterrissage d'un planeur à aile fixe sur des surfaces verticales [20], mentionnés précédemment, ont fait usage d'un contrôle feedforward pour la manoeuvre et d'un capteur de distance pour détecter le mur. Cette approche est intéressante, car l'algorithme est suffisamment simple pour être exécuté par un processeur embarqué et un système de détection minimaliste ne nécessitant même pas de centrale inertielle (IMU). Par contre, ceci n'a pas pu être appliqué avec succès à un drone motorisé, en raison du poids additionnel que représente un système de propulsion ajouté à un planeur. Plus précisément, l'approche proposée pour atterrir consistait à arrêter le moteur au moment d'initer la maneouvre d'atterrissage. Le moteur devenait simplement une masse additionnelle à soutenir lors de la manoeuvre de transition du vol horizontal à une orientation verticale. Ainsi, les forces d'impact à l'atterrissage devenaient plus grande que pour le cas d'un planeur. Pour le même train d'atterrissage, ces forces d'impact étaient donc trop grandes pour assurer une adhésion à la surface.

Figure 2.7 Manoeuvre d'atterrissage du planeur du BDML [20].

Enfin, les travaux de Green et al. [8] présentent un contrôle en boucle fermée (PID) sur les surfaces de contrôle d'un UAV à aile fixe, pour réaliser une transition du vol horizontal vers un vol stationnaire vertical. Ainsi, l'algorithme de contrôle peut être exécuté par un processeur embarqué et un IMU est suffisant pour l'estimation de l'état du système. La méthode présentée pour le contrôle du moteur nécessite quant à elle l'ajout de capteurs à ultrasons (Fig. 2.8), pour le maintien d'une altitude fixe. En effet, il est pris en compte que la surface horizontale est plate sous le drone et que l'altitude de celui-ci est faible (moins de 10 mètres). Cette approche n'est donc pas applicable dans le projet présenté. Les applications visées requièrent d'être robuste à des atterrissages dans un environnement au relief accidenté et pour des altitudes plus élevées, afin d'atteindre des points d'observation d'intérêt.

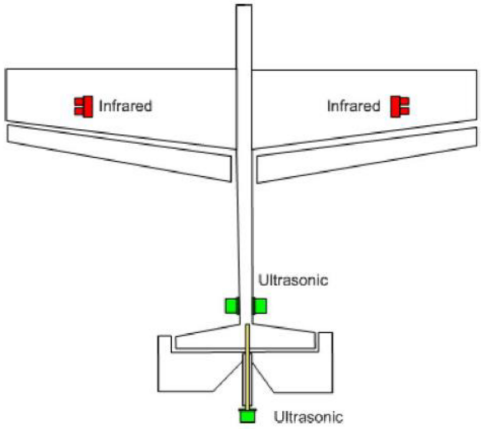

Figure 2.8 Disposition des capteurs à ultrasons (carrés verts) sur le drone à aile fixe de Green et al. [8].

Une solution de contrôle envisageable pour le projet présenté est une combinaison entre les deux précédentes méthodes. En effet, les deux méthodes montrent que des systèms embarqués peuvent permettre de détecter des murs et réaliser un contrôle robuste pour des manoeuvres de précisions (ex. : vol vertical stationnaire). Notamment, comme la précision de la position finale de l'atterrissage n'est pas importante, des capteurs à ultrasons comme ceux utilisés par Green et al. (mesure d'altitude précise) ne sont pas nécessaires. Or, comme il faut limiter les vitesses d'impact verticales et horizontales, les données mesurées par une centrale inertielle peuvent être utilisées pour réaliser un contrôle en boucle-fermée. Plus particulièrement, des données d'accéléromètres et de gyroscopes permettraient de contrôler (1) l'orientation de l'avion, à travers des déflections de surfaces de contrôle, et (2) la vitesse verticale suite à une manoeuvre de cabrage (orientation verticale), en variant la commande envoyée au système de propulsion.

2.4 Conclusion

Une revue de l'état de l'art permet de conclure qu'aucun robot n'est capable de réaliser de façon autonome (sans intervention humaine) une mission impliquant des étapes d'atterrissage, décollage et grimpe de surfaces verticales. Plus particulièrement, aucun avion à aile fixe motorisé n'est capable de compléter à la fois des atterrissages et décollages verticaux. Or, les avions sont intéressants pour ce type de tâches, en raison de leur efficacité pour des déplacements sur de longues distances. Pour mettre au point un avion capable de réaliser des atterrissages et décollages verticaux, une technologie d'adhésion doit d'abord être sélectionnée. Les microgriffes sont une option intéressante en raison notamment d'une grande robustesse, par rapport à des technologies comme les adhésifs inspirés du Gecko. Le contrôle de manoeuvres d'atterrissage et de décollage peut quant à lui être réalisé entièrement à l'aide de systèmes embarqués. Entre autres, des capteurs répandus pour le contrôle de drones (ex. accéléromètres, gyroscopes, etc.) peuvent permettre d'assurer que l'avion maintienne de basses vitesses au moment de toucher un mur. Une intégration efficace du train d'atterrissage permettrait également de grimper sur des murs, en utilisant la poussée du moteur. L'orientation favorable du véhicule en position perchée (moteur pointant vers le haut) permettrait ainsi de diminuer le temps de transition entre un mode perché et un mode de grimpe, présentant une manoeuvre de grimpe potentiellement plus efficace que la grimpe avec des pattes actionnées.

CHAPITRE 3

ATTERRISSAGES ET DÉCOLLAGES VERTICAUX ASSISTÉS PAR LA POUSSÉE AÉRODYNAMIQUE

Avant-propos

Auteurs et affiliation :

- D. Mehanovic : étudiant à la maîtrise, Université de Sherbrooke, Département de génie mécanique
- J. Bass : étudiant à la maîtrise, Université de Sherbrooke, Département de génie mécanique
- T. Courteau : étudiant à la maîtrise, Université de Sherbrooke, Département de génie électrique
- D. Rancourt : professeur, Université de Sherbrooke, Département de génie mécanique
- A.L. Desbiens : professeur, Université de Sherbrooke, Département de génie mécanique

Date d'acceptation : 28 avril 2017

État de l'acceptation : Version finale publiée

Revue : Lecture Notes in Computer Science : Living Machines 2017 - Biomimetic and Biohybrid Systems

Référence : [22]

Titre français : Atterrissages autonomes d'un drone à aile-fixe sur des surfaces verticales

Contribution au document : Cet article contribue au mémoire en présentant la méthode d'atterrissage développée, de mêmes que les modèles numérique et tests utilisés pour implémenter la méthode dans un prototype de drone. La méthode de décollage est également détaillée.

Résumé français : Nous présentons le premier drone à aile-fixe capable de se percher de façon autonome sur des surfaces verticales et d'en décoller. Inspiré par les

oiseaux, cet avion utilise une manoeuvre de cabrage assistée par la poussée pour rapidement ralentir avant de se poser. Des microgriffes sont utilisées pour permettre à l'avion de s'accrocher à des surfaces rugueuses, alors que le contrôle de la manoeuvre est entièrement embarqué. L'effet de la poussée aérodynamique sur l'enveloppe d'atterrissage de l'avion est analysée et un contrôleur de vitesse verticale est proposé pour créer des descentes fluides et robustes vers un mur. Plusieurs atterissages ont été testé, à travers une plage de conditions de vol (vidéo du S-MAD disponible : http ://createk.recherche.usherbrooke.ca/LM2017/).

Lecture Notes in Computer Science, Volume 10384, July 2017

Autonomous Thrust-Assisted Perching of a Fixed-Wing UAV on Vertical Surfaces

Dino Mehanovic, John Bass, Thomas Courteau, David Rancourt, Alexis Lussier Desbiens

3.1 Abstract

We present the first fixed-wing drone that autonomously perches and takes off from vertical surfaces. Inspired by birds, this airplane uses a thrust-assisted pitch-up maneuver to slow down rapidly before touchdown. Microspines are used to cling to rough walls, while strictly onboard sensing is used for control. The effect of thrust on the suspension's landing envelope is analyzed and a simple vertical velocity controller is proposed to create smooth and robust descents towards a wall. Multiple landings are performed over a range of flight conditions.

Index Terms – Perching, Multimodal, Scansorial, Fixed-Wing, UAV, Drone

3.2 Introduction

The increasing demand for civil applications of unmanned aerial vehicles (UAV) is encouraging the development of small platforms with extended mission life. However, small airframes have low aerodynamic efficiency and reduced energy storage capabilities, both of which severely limit the endurance and range of these platforms. In nature, many small birds, insects and mammals regularly land to rest, feed, seek shelter or stealthily monitor an area.

Recently, a variety of bioinspired robotic platforms have been created for perching and are reviewed in detail in[38]. Among those, quadrotors have been used due to their ability to perform agile flight trajectories to slow down before impact [29, 41]. Directly flying into targets has also been explored by appropriately positioning adhesives on fixed-wing and multi-rotor airframes [3, 7, 13, 18]. To perform both perching and climbing on vertical surfaces, the SCAMP quadrotor re-orients itself after flying directly into a wall [33].

The implementation of such perching capabilities in a powered fixed-wing UAV remains a challenge for various reasons (e.g., added mass by propulsion system). Thus, the most successful solutions are based on glider platforms unable to take off [16, 19, 26]. Notably, the perching trajectory for the Stanford Perching Glider is inspired by the flying squirrel

Figure 3.1 Many birds exhibit landing trajectories with high body pitch angles and significant upward force to maintain a horizontal approach. Courtesy of : Maxis Gamez (a), PCO (b), Warren Photography (c) and Kaddy (d).

[19]. It performs a pitch-up maneuver followed by a drag-affected ballistic phase, before adhering to vertical surfaces with microspines. However, the ballistic phase creates only a short zone of suitable touchdown conditions that impose severe requirements on the platform's wall sensor, as discussed further in Section 3.3.

Sherbrooke's Multimodal Autonomous Drone (S-MAD), presented in this paper, draws inspiration from nature in order to perform full cycles of landing, standby, takeoff and flight (LSTF). As illustrated in Figure 3.1, many birds use high body pitch angles and significant upward force to maintain horizontal perching approaches. This paper demonstrates that such a thrust-assisted landing strategy, when utilized on a fixed-wing aircraft, enables controlled steady-state descents (SSD) towards perching sites. This reduces the impact speed and significantly extends the zone of suitable touchdown conditions, leading to enhanced reliability and reduced hardware requirements (e.g., suspension, wall sensing). This landing strategy also enables simple takeoff, facilitated by the favorable thrust orientation while perched. To our knowledge, this is the first autonomous fixed-wing platform capable of performing both perching and takeoff maneuvers.

3.3 Perching Strategy Overview

The thrust-assisted perching maneuver described in this paper builds onto previous work that enabled a fixed-wing glider to perch on vertical surfaces following a rapid feedforward pitch-up maneuver [20]. This maneuver, illustrated by the dotted line in Figure 3.2, rapidly slows down the glider and exposes the landing gear to the vertical surface. As the glider reaches full pitch-up, the velocity is reduced to such an extent that aerodynamic forces become negligible and the glider keeps travelling on a mostly ballistic trajectory

towards the wall. With proper timing, the airplane touches down with a sufficiently low speed to allow a suspension to dissipate the remaining kinetic energy, while favoring the feet attachment to the surface. This approach leads to high success rates on airframes with low wing loading, even with the use of a simple feedforward controller [19]. However, increasing the mass of the platform with additional payload and motors causes the suspension touchdown envelope (i.e., the set of touchdown states that lead to successful landing) to shrink down to negligible size. At the same time, the increased wing loading makes it more challenging to reduce the forward velocity to acceptable levels, before gravity significantly increases the vertical velocity to unacceptable values. Thus, as the mass increases, fewer trajectories can bring the glider from normal flying conditions to the suspension's touchdown envelope, leading to reduced success rate.

Comparatively, the approach described in this paper takes advantage of thrust to control the final vertical and forward velocities such that :

1. Suitable touchdown conditions are available during an extended distance to reduce the timing and sensing requirement needed to trigger the maneuver.
2. Lower impact speeds are experienced by the suspension, leading to size and mass reduction.
3. Approach trajectories that favor adhesive engagement can be used.
4. Control authority is maintained throughout the full maneuver due to the propeller flow on the control surfaces. This allows early termination of the perching maneuver and recovery until the final stages of the maneuver.
5. Takeoff is possible, enabling repeated cycles of LSTF during a single mission.

The final approach of both gliding and thrust-assisted trajectories can easily be compared conceptually from the apex conditions (i.e., $v_x = v_{x_{apex}}$, v_y=0), by assuming limits on the allowable velocity at landing (i.e., $0 < v_x < v_{x_{max}}$ and $v_{y_{min}} < v_y < 0$). In the case of the glider, velocity as a function of time and distance travelled while maintaining suitable touchdown states (Δx_s) can be calculated by assuming a ballistic trajectory, as expressed in Figure 3.2. Comparatively, the post-apex steady-state trajectory of the thrust-assisted maneuver can be described by assuming a constant pitch (q), and by equating the vertical thrust component to mg and the horizontal component to the drag ($1/2\rho C_D A v_x^2$). Velocities and distance travelled while maintaining suitable touchdown states are described in Figure 3.2.

As expected, thrust-assisted perching allows the designer to specify the velocity at touchdown given (1) the physical parameters mg/A, (2) the commanded pitch approach angle

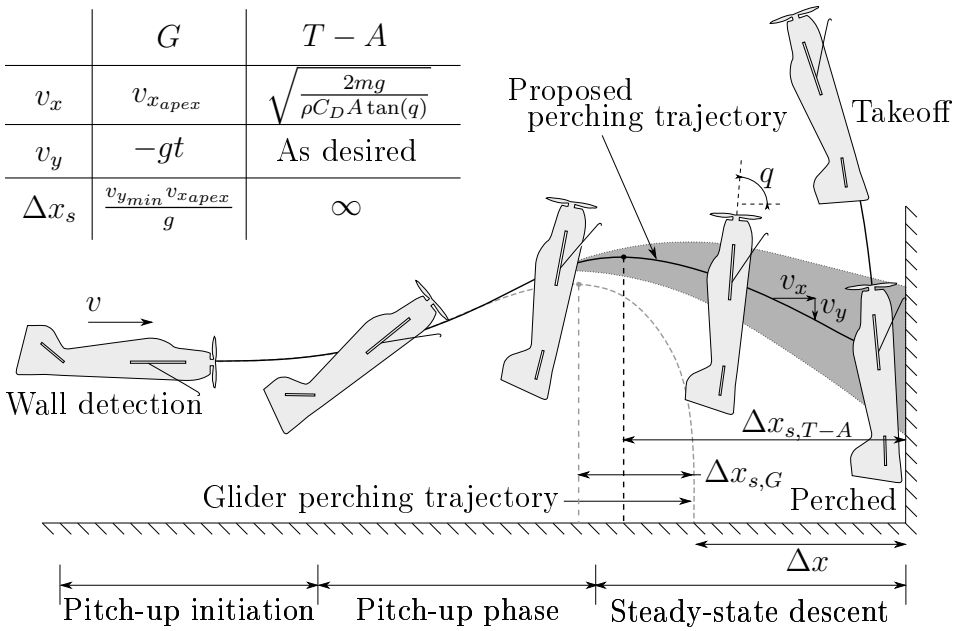

	G	$T-A$
v_x	$v_{x_{apex}}$	$\sqrt{\frac{2mg}{\rho C_D A \tan(q)}}$
v_y	$-gt$	As desired
Δx_s	$\frac{v_{y_{min}} v_{x_{apex}}}{g}$	∞

Figure 3.2 Representation of the proposed thrust-assisted ($T-A$) perching strategy and comparison to a glider (G) trajectory. Variations in SSD's velocity slope, e.g., induced by sensor bias or battery level, are represented by the shaded area. Post-apex velocities and Δx_s shown in the top-left table, where g is the gravitational acceleration and t is time. Allowable wall detection error gain for $T-A$ over G is identified by Δx.

(q) and (3) assuming that v_y can be measured and controlled through thrust. Under these conditions, the airplane can travel an indefinite distance in states suitable for touchdown. This is an important gain over the gliding maneuver, for which the Δx_s distance is on the order of 20 cm and thus imposes strict sensing requirements.

However, the addition of thrust also adds some challenges. Indeed, any remaining thrust at impact (e.g., propeller spin down after touchdown detection through onboard accelerometer) significantly modifies the touchdown envelope by reducing the shear forces experienced by the microspines and the corresponding adhesion. Thrust-assisted landing is also highly sensitive to numerous airframe parameters and initial flight conditions, reducing the success rate achievable by a simple feedforward maneuver. The following sections describe the implementation of thrust-assisted perching, analyze the effect of thrust on the touchdown envelope and propose a novel simple feedback controller based on vertical velocity.

3.4 Implementation

The airframe used in the experiments described in this paper is presented in Figure 3.3. It consists of a modified McFoamy airplane (i.e., 12 A ESC, Turnigy 2730 1500 kV motor and

8x6 propeller for a static thrust-to-weight ratio of 1.5), combined with a 3DR PixHawk autopilot for onboard control. This autopilot integrates most required sensors required for vertical velocity estimation and impact detection (gyro, accelerometers, barometer), and communicates with a lightweight laser rangefinder (TeraRanger One) for wall detection. Custom control loops run onboard the PixHawk at 200 Hz.

Five microspines are used on each foot to attach onto vertical surfaces. Although various adhesion strategies exist [40], microspines are preferred due to their proven performance on numerous rough surfaces of interest (e.g., stucco, concrete, brick, roofing shingles) [1]. Inspired by insect feet, the microspines (Figure 3.3) consist of hooks that attach to rough vertical surfaces through mechanical interference and friction, while distributing the load uniformly between asperities. As illustrated in Figure 3.3, the microspines require shear and normal force loadings within a safe zone delimited by friction, adhesion and overload limits to remain attached to the surface.

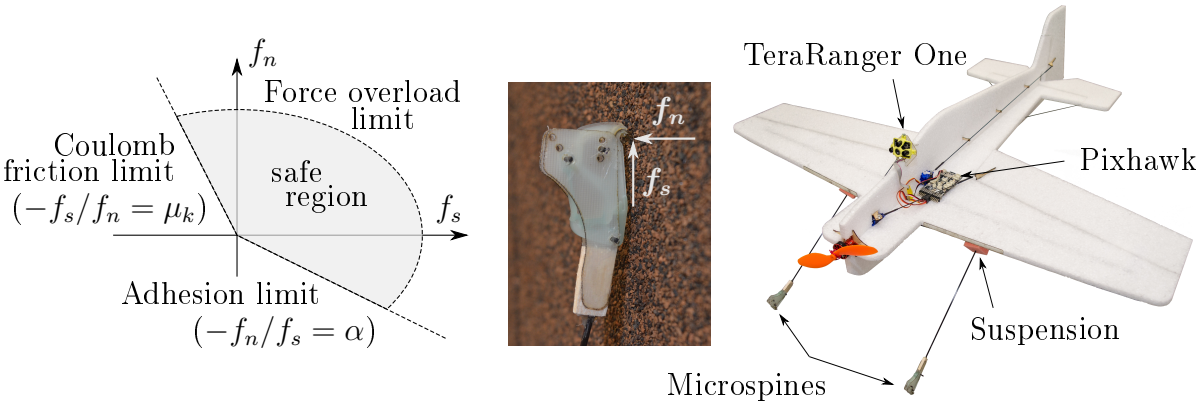

Figure 3.3 Safe force region, microspines and platform components.

A suspension is installed between the airplane and the microspines to help bring the platform to rest, while favoring attachment to the surface. The suspension requirements for a thrust-assisted perching airplane are simplified due to the low touchdown speeds and the controlled touchdown direction. The proposed perching mechanism consists of a flexible beam, anchored in the airframe's wing and damped by a urethane foam block. At 18 g, the resulting suspension is significantly simpler and lighter than the suspension of the Stanford Perching Glider (28 g). Overall, with the added mass of the TeraRanger (15 g), the components required to enable perching only account for 10% of the platform's total mass (320 g).

3.5 Thrust-Assisted Touchdown Envelope

As discussed previously, the remaining thrust force during landing affects the touchdown envelope by reducing the shear force exerted at the feet and, incidentally, the adhesion available. This section describes the model developed to analyze the landing forces, its validation and the resulting landing envelope when thrust is present.

3.5.1 Model description

The thrust-assisted perching maneuver described in this paper consists of mostly sagittal motion, with complex behaviors of the microspines at the feet. To properly represent this system, a hybrid planar dynamic model of the airplane and suspension is used, with both sliding and sticking states possible at the feet. By calculating the forces created during landing, and verifying if either the adhesion or the overload limit is reached, this model can predict the success or failure of different landing conditions.

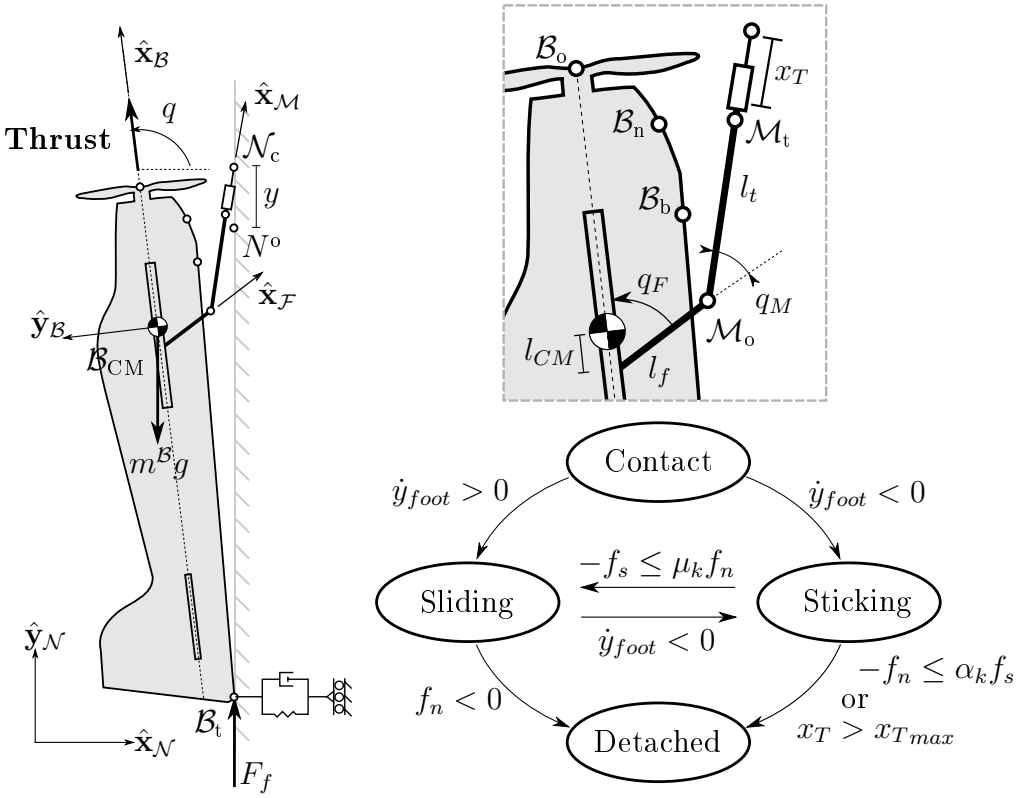

Figure 3.4 System geometry, reference frames, forces and model transitions.

Figure 3.4 illustrates the geometry and forces defining the system, as well as the hybrid model states and discrete events leading to transitions. Besides the new suspension and added thrust, the model structure and contact dynamics at nose, belly and tail are similar to [19]. The airplane is modeled as a rigid body $\mathcal{B}$ and the legs are described by a single

leg and foot. The combination of the leg's flexible beam and memory foam is modeled as a pseudo-rigid body [12], where two rigid segments (i.e., the fixed femur, $\mathcal{F}$, and the moving tibia $\mathcal{M}$) are connected by a pivot (knee) with lumped torsional stiffness and damping parameters. The foot is approximated by a linear spring-damper system. The thrust force is defined as a constant value ($m^{\mathcal{B}}g$) until impact detection (i.e., 14 m/s^2 acceleration at CG). From that point, it follows an exponential decrease with an experimentally validated time constant of 85 ms. Due to the relatively low impact speed, the aerodynamic forces are neglected in this model. The contact point model at the foot can either take the form of a rolling joint (sliding) or a pin joint (sticking), depending on force and motion conditions at the foot, as described in the lower right transition diagram in Figure 3.4.

Furthermore, as shown in Figure 3.4, various reference frames and variables are introduced for the analysis. Without going into the details, it is easy to express the position of the airplane's center of mass ($\mathcal{B}_{\mathrm{CM}}$) as :

$$\mathbf{r}^{\mathcal{B}_{\mathrm{CM}}/\mathcal{N}_{\mathrm{t}}} = y\hat{\mathbf{y}}_{\mathcal{N}} - (x_T + l_t)\hat{\mathbf{x}}_{\mathcal{M}} - l_f\hat{\mathbf{x}}_{\mathcal{F}} + l_{CM}\hat{\mathbf{x}}_{\mathcal{B}} \tag{3.1}$$

This vector, and other easily expressed quantities, can be used to establish the equations of motion through Kane's method for each generalized speed u_r [25]. The sliding foot model uses $\dot{q}$, $\dot{q}_M$ and $\dot{y}$ as generalized speeds (i.e., x_T is constant), while the sticking foot model uses $\dot{q}$, $\dot{q}_M$ and $\dot{x}_T$.

3.5.2 Model validation

To confirm that the proposed model can accurately represent a wide range of touchdown conditions, four landings were performed by hand throwing the airplane without thrust on an instrumented force plate. Representative touchdown speeds of 1-2 m/s were used in various directions, as illustrated in Figure 3.6, resulting in different loading trajectories that excite the full system dynamics. During these tests, constant pitch ($q = 86 \pm 3°$) and angular velocity ($\dot{q} = -50 \pm 30°/\mathrm{s}$) were maintained, similar to the commanded states at touchdown.
The experimental setup used to measure shear and normal forces consists of a fabric-covered plate. This surface is used to guarantee simultaneous engagement of all microspines with the surface. The plate is instrumented using an ATI Mini40 force/torque sensor sampled at 1 kHz. The plate has a resonance frequency of at least 150 Hz in all directions. The recorded data is post-filtered using a 20 Hz Butterworth filter (20th order, zero-phase) to remove the structural modes of the airframe. The touchdown states are measured at 200 Hz using a motion capture system. Figure 3.5 shows the results for two tests.

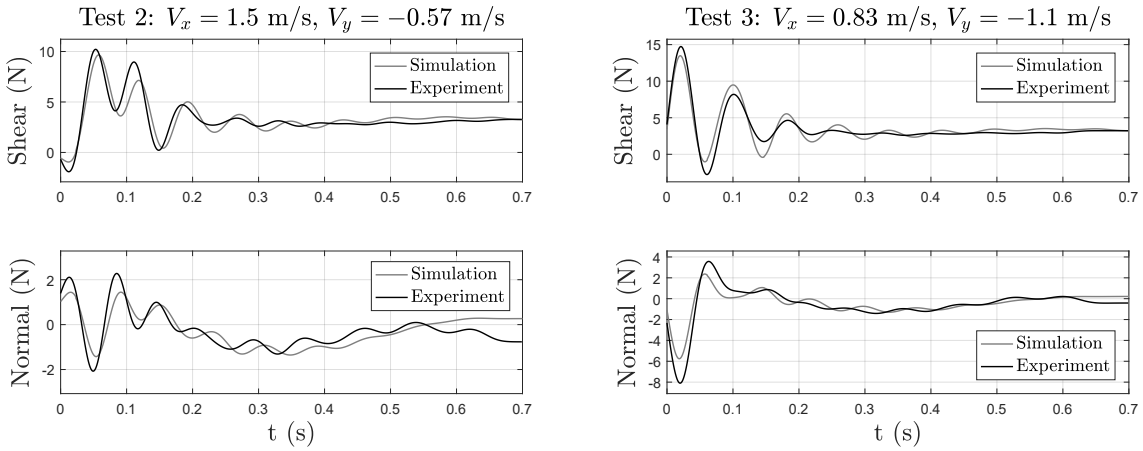

Figure 3.5 Shear (f_s) and normal (f_n) forces acting on microspines at landing as obtained from simulations and experiments for tests 2 (left) and 3 (right).

Some physical parameters of the model were identified from the measured forces with a genetic algorithm (GA). To do so, the GA varies the selected physical parameters over a predefined range, aiming at minimizing the first 0.4 seconds of the normalized RMS (NRMS) error for shear and normal force in all four tests. The RMS error of each landing is normalized by its maximum absolute force range to produce a representative fit over different impact conditions. Each generation contains 100 individuals and the GA stops after the NRMS change over 5 generations is less than 0.01%. This condition was reached after 12 generations, with the NRMS error for all tests being less than 0.5%. The best parameters found with the GA are listed in Table 3.1.

Tableau 3.1 Physical properties of the system

Parameter	**Symbol**	**Value**	**Source**
Mass	$m^{\mathcal{B}}$	0.32 kg	Measured
Inertia	I_{zz}	0.017 kg m^2	GA
Pseudo-rigid body factor	γ	0.93	GA
Leg length	L	0.317 m	Measured
Femur and tibia length	l_f, l_t	0.022 m, 0.295 m	$(1-\gamma)L$, γL
Knee stiffness and damping	k_k, c_k	1.26 Nm/rad, 0.057 Nms/rad	GA
Foot stiffness and damping	k_f, c_f	2120 N/m, 5.32 Ns/m	GA
Wall stiffness and damping	k_w, c_w	231 N/m, 73 Ns/m	GA
Femur angle from fuselage	q_F	-30°	Measured
Spines natural length	l_0	0.0036 m	Measured

The suspension's physical parameters obtained with the GA correspond to expected results : the inertia is slightly higher than our CAD model while the foot stiffness/damping are comparable to the results presented in [19]. The wall stiffness value is also significantly lower due to the softer nature of the EPP foam used on this airplane.

3.5.3 Landing State Map (LSM)

The calibrated model can be used to identify the envelope of impact states that lead to successful perching, as shown in Figure 3.6. The LSM itself is validated with landings on a wall covered with asphalt shingles (i.e., $f_n/f_s < 1$). The platform is hand-thrown at various velocities, with angular speed and pitch angle maintained relatively constant. A total of 35 trials were performed as illustrated in Figure 3.6, including six failures outside of the predicted success area. Slow-motion footage confirmed that these failures occurred through microspines overload, as predicted by the model.

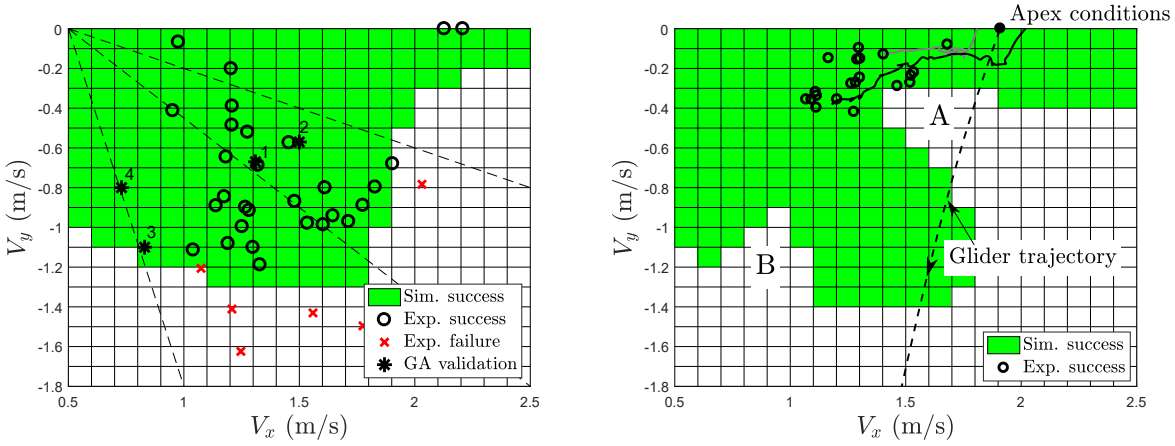

Figure 3.6 Simulated LSM in green, with (right) and without (left) thrust. Simulations are performed with 5 spines engaged. (left) Experimental landings validating the simulated LSM ($q = 86 \pm 3°$, $\dot{q} = -50 \pm 30°/s$). Similar shear and normal force patterns are created for loading trajectories along the same radial dashed line. This reduces the number of necessary GA validation points for model calibration. (right) Touchdown velocity of 20 thrust-assisted approaches from horizontal flight. Two approach trajectories are also illustrated.

This model can further be used to predict successful perching conditions when thrust is still present following touchdown (right LSM in Figure 3.6). This LSM was calculated by considering the variable delay introduced by detecting the foot impact with the accelerometer located on the airplane's body, given the soft suspension, and by considering the motor spin-down. These effects significantly reduce and reshape the LSM's area (e.g., zone A in Figure 3.6).

3.6 Perching Controller Design

The proposed pitch-up trajectory takes advantage of the airframe's high thrust-to-weight ratio to significantly extend the suitable horizontal distance available for perching. However, thrust creates disturbances not present on a glider. These include yaw perturbation

due to gyroscopic effect during pitch-up and roll perturbation, caused by the rotor torque required to accelerate the propeller at the entry of the SSD phase. To compensate for these perturbations, three decoupled PD feedback loops are used for each control surface [8, 20]. Thrust-assisted perching is also difficult to perform under a feedforward control architecture. Indeed, small variations in initial battery voltage, airplane mass, CG position and launch speed all lead to large variations in the touchdown velocity and, consequently, failure to land as detailed in Table 3.2. The remainder of this section details a simple thrust controller, compares the results with feedforward control and describes tuning of the controller through the use of a classifier.

3.6.1 Thrust Control over Vertical Velocity (TCV^2)

To create the desired SSD phase favoring smooth landings under a wide range of conditions, the proposed thrust controller (TCV^2) utilizes a proportional feedback loop over RPM to maintain a desired vertical speed from wall detection. This feedback term is added to a constant command ($T_o \simeq mg$) as follows :

$$T_c = K_p(V_d - V_m) + T_o \tag{3.2}$$

where T_c is the output thrust, K_p is a proportional gain, V_d is the desired vertical speed, V_m is the measured vertical speed and T_o is the constant thrust command. The vertical speed is calculated through integration of the acceleration, starting from the Pixhawk estimate during horizontal flight.

Simulations are used to compare the TCV^2 and feedforward controller robustness by individually varying a set of nine variables that include airframe, actuator and sensing parameters, along with initial condition variations (fixed wall detection distance of 5.5 m). To capture the dynamics of the complete perching maneuver, this study combines a flight dynamics model developed by Khan et al. [14] with the hybrid perching model described in Section 3.5. The selected flight dynamics model captures various important aspects of the proposed perching maneuver, e.g., unsteady and high-alpha aerodynamics, effects of control surface deflections and propeller slipstream effects.

The results, presented in Table 3.2, demonstrate the advantages of TCV^2 over a feedforward controller. The most sensible parameters for a feedforward controller are mass and battery level. If these parameters are not carefully tuned, the thrust and gravity forces are unbalanced and the vertical velocity varies throughout the maneuver. Changing the CG position also modifies the capability of the airplane to rapidly pitch-up, thus affecting the

Tableau 3.2 Varied parameters and success range for each controller (FR : Full range)

Parameter	Units	Baseline	Range	Feedforward	TCV^2
V_x (body-fixed frame)	m/s	8	[6 ; 10]	[7.1 ; 8.6]	FR
V_z (body-fixed frame)	m/s	0	[-2 ; 2]	FR	FR
Pitch	°	0	[-20 ; 20]	[-16.8 ; 20]	FR
Mass	kg	0.32	[0.28 ; 0.36]	[0.31 ; 0.34]	FR
Inertia	kg m2	0.017	[0.012 ; 0.012]	FR	FR
Angular Velocity	°/s	0	[-57 ; 57]	FR	FR
Range sensor error	m	0	[-0.3 ; 0.3]	[-0.3 ; 0.26]	FR
CG position*	cm	-31.3	[-33.3 ; -29.3]	[-31.3 ; -29.6]	[-31.3 ; -29.9]
Battery level	%	100	[80 ; 100]	[96 ; 100]	FR
Accelerometer bias	m/s^2	0	[-0.1 ; 0.1]	-	FR

distance required to perform the maneuver. As expected, the TCV^2 feedback controller compensates for variations of almost all of these parameters.

3.6.2 TCV^2 proportional gain sizing

A more thorough analysis is required to tune the controller for maximum success rate, given simultaneous variations of the identified parameters over their allowable range (Table 3.2). To speed up the analysis, a support vector machine (SVM) classifier that evaluates the combinations for successful landing is trained on the complete numerical model, which includes the aircraft's dynamics during flight and after impact with the wall. This classifier is trained using 30,000 simulations designed using a Latin hypercube sampling method. A set of 85% of these simulations is used for training and 15% for validation. Defining the SVM's Gaussian radial basis function kernel with $\sigma = 1.4$ in the normalized space, a prediction accuracy of 92.8% is achieved for the validation set. The success rate is evaluated for each K_p, assuming a uniform distribution of other parameters over their respective range.

The results of this analysis, shown in Figure 3.7, reveal that a K_p value of approximately 0.5 leads to the highest probability of successful perching for the parameter variations described in Table 3.2. This probability rapidly decreases for lower K_p. A small proportional gain also introduces considerable increases in altitude - up to 6 m, as full thrust is applied throughout the full maneuver. Similarly, increasing the K_p value leads to excessively low thrust commands during the pitch-up phase which slows down the transition to SSD. This decreases the probability of success given a fixed wall detection distance.

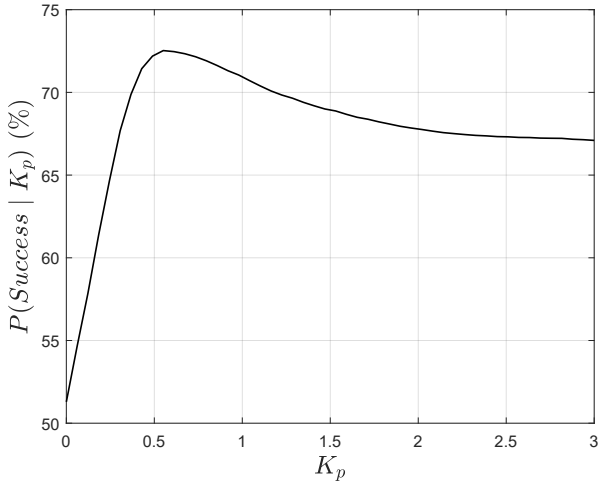

Figure 3.7 Success probability of the perching maneuver for a known K_p.

3.7 Experimental Results

A series of tests were conducted on the platform presented previously. The airplane was launched towards a vertical wall covered with asphalt shingles at speeds ranging from 6.7 to 7.7 m/s. A total of 20 consecutive launches were performed, for which a 100% success rate was achieved. The touchdown velocities of these tests are mapped on the LSM (right) in Figure 3.6, with two trajectories showing that the airplane maintains vertical descent speeds around the commanded value (-0.2 m/s). A typical landing is illustrated in Figure 3.8. After such landing, the airplane can use its thrust to take off vertically as described in [20].

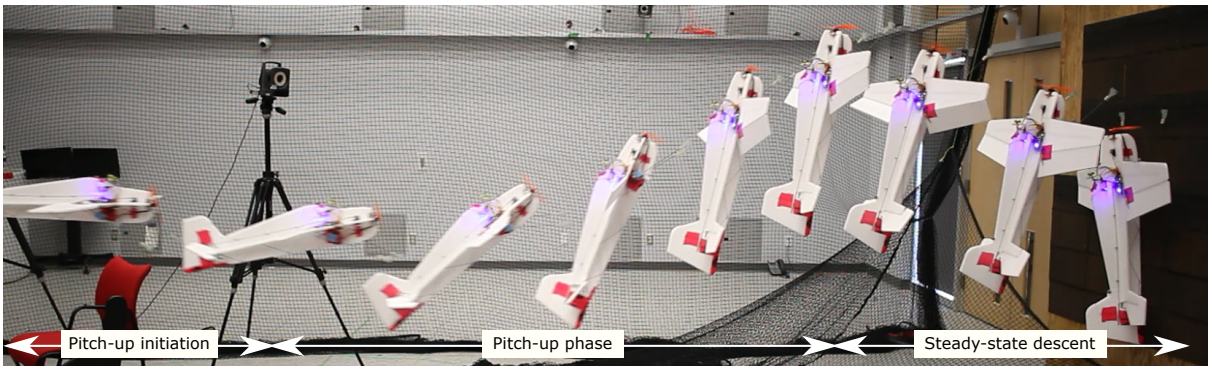

Figure 3.8 Sequence of the thrust-assisted perching maneuver.

3.8 Conclusion and Future Work

This paper introduces S-MAD, the first fixed-wing UAV capable of thrust-assisted perching and takeoff. This small aerobatic platform performs a pitch up maneuver to rapidly slow down and expose its landing gear to vertical surfaces. A PixHawk controller samples the onboard sensors, including a laser range finder, and executes custom control loops to perform the maneuver autonomously.

Future work includes various improvements on the system, such as a more precise estimation of the vertical velocity and a mass reduction of the suspension. An important enhancement will also be the inclusion of non-contact sensors to turn off the propeller preemptively by early detection of incoming touchdowns. In the longer term, it is expected that this configuration of actuators, electronics and sensors will allow thrust-assisted wall climbing, aborted approaches and recovery from failed attachment.

The ability to perch reliably on vertical surfaces opens the door for repeated cycles of landing, standby, takeoff and flight. This enables extended mission durations for small UAVs, offering new types of applications. Ultimately, such bird-inspired platforms could be used for long duration surveillance, energy harvesting, inspection of structures or reconfigurable sensor networks.

CHAPITRE 4

PRINCIPES DE CONCEPTION POUR DES ROBOTS MULTIMODALS EFFICACES

Avant-propos

Auteurs et affiliation :

- D. Mehanovic : étudiant à la maîtrise, Université de Sherbrooke, Département de génie mécanique
- D. Rancourt : professeur, Université de Sherbrooke, Département de génie mécanique
- A.L. Desbiens : professeur, Université de Sherbrooke, Département de génie mécanique

Date d'acceptation : –

État de l'acceptation : En révision

Revue : IEEE Robotics and Automation Letters

Référence : [23]

Titre français : Grimpe robotique rapide et efficace

Contribution au document : Cet article contribue au mémoire en présentant l'analyse et l'implémentation d'une méthode de grimpe aérienne de surfaces verticales avec un avion à aile-fixe.

Résumé français : Nous présentons un drone percheur utilisant sa poussée aérodynamique pour girmper le long de surfaces verticales. La vitesse et l'efficacité de la manoeuvre de grimpe du robot sont comparées avec celles de différents grimpeurs aériens et grimpeurs à pattes. Des modèles aérodynamiques sont utilisés pour prédire les performance de l'avion dans plusieurs régimes de grimpe aérienne, et sélectionner un contrôleur pour le maintien d'une distance fixe avec un mur en montée verticale. La manoeuvre est testée à l'intérieur et à l'extérieur, pour des grimpes courtes et longues.

IEEE Robotics and Automation Letters

Fast and Efficient Robotic Climbing

Dino Mehanovic, David Rancourt, Alexis Lussier Desbiens

4.1 Abstract

We present a perching UAV that uses aerodynamic thrust to climb along vertical surfaces. The speed and efficiency of the robot's climb maneuver are compared with those of existing legged and aerial climbers. Aerodynamic models are used to predict the robot's performance in various aerial climb regimes, and select a controller for wall distance tracking in vertical flight. The maneuver is tested indoor and outdoor, for both short and long climbs.
Index Terms – Perching, Multimodal,, Fixed-Wing, UAV, Climbing, Robot

4.2 Introduction

The ability to perch on vertical surfaces enables unique applications for small UAV's. It eliminates the need for continuous flight while performing observation or sensing tasks, drastically reducing power consumption. Perching strategies for aerial platforms have therefore been a subject of interest in recent years [38]. Among the numerous robots that were developed, only quadrotors were able to repeatedly perform perching and takeoff [13, 33]. Completing both tasks with a motorized fixed-wing platform remained a challenge, notably due to added mass from the propulsion system increasing loads at wall impact [20].

However, the authors have recently demonstrated both perching and takeoff abilities with the S-MAD (Sherbrooke's Multimodal Autonomous Drone), a motorized fixed-wing UAV [22]. The S-MAD uses a landing gear with microspines [1] to cling to rough surfaces, and takes advantage of its propulsion system to create an upward force while approaching a wall. This landing approach ensures low velocities at impact and therefore reduces loads on the landing gear, while favoring the engagement of the microspines. Previous fixed-wing perching strategies turned off the motor in flight, resulting in an essentially ballistic trajectory at touchdown [20]. The developed system configuration enables simple aerial maneuvers to climb vertical surfaces, and perform precise relocation after landing. Indeed, the S-MAD's motor orientation when perched is favorable to simple, thrust-assisted takeoffs (Fig. 4.1), allowing fast transitions between a perched state and flight. As detailed further, this leads to effective thrust-based climbing (Fig. 4.2e). For even more efficient climbing, the S-MAD can also transition to conventional fixed-wing flight to generate a lift

Figure 4.1 Autonomous thrust-assisted climbing of an outdoor brick wall. A total distance of 5 meters was covered.

force with its wing (Fig. 4.2d). Selecting one specific maneuver to reduce the energetic cost of climbing is therefore non-trivial, as the optimal configuration can be anywhere between horizontal and strictly vertical flight.

Other wall climbing strategies have also been demonstrated previously. For example, actuated legs have been implemented in many small robotic climbers, as reviewed in [40]. Such legged robots typically use quasi-static locomotion [5, 10, 11, 15, 28, 33] (Fig. 4.2a), which requires frequent operation of the motors outside its peak-efficiency due to the acceleration/deceleration of the body and legs. In order to avoid such losses and climb faster, other legged platforms have relied on dynamic climbing gaits (Fig. 4.2b), taking advantage of planar yaw dynamics of their body to operate actuators at peak efficiency [21, 24, 35]. Climbing with wheels or tracks can also allows peak efficiency operation [39] (Fig. 4.2c). A wheeled platform relying on thrust for upward motion and for maintaining contact with the wall has also been developed [2] (Fig. 4.2g). Quadrotor-based climbing robots have also been demonstrated by a few teams [13, 33] (Fig. 4.2f).

These different climbing strategies, as implemented on existing robots, are compared in Section 4.3 on the basis of climb speed and specific resistance. Another metric for system integration is also used to quantify the interest of using aerial climbing on the S-MAD. Further, the selection, implementation, and testing of a specific aerial climbing maneuver are presented in Section 4.4 and 4.5. Experimental results are then presented in Section 4.6 to quantify the system's climbing efficiency.

4.3 Robotic climbing performance

The design of a multimodal robot imposes various challenges, as efficient operation is required in modes that are potentially completely decoupled. In S-MAD's case, aerial climbing along walls is implemented with only a small additional amount of mass, taking advantage of a favorable integration of landing gear and perching ability. Using metrics to quantify system integration and climbing efficiency, S-MAD is analyzed and compared with other robotic platforms.

4.3.1 System integration

Recent studies have proposed ways to quantify the price paid for the integration of multiple modes in a single platform [30]. In [43], a mass integration metric allows insight into the amount of mass shared among independent modes,

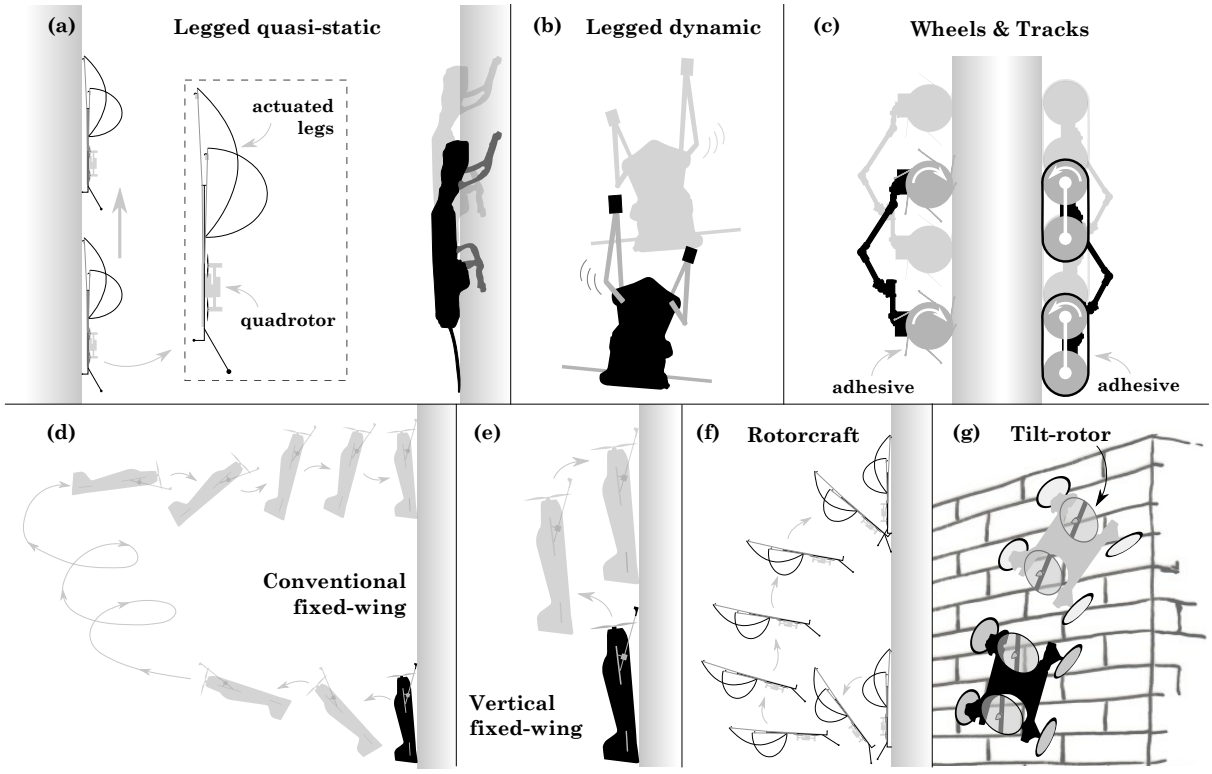

Figure 4.2 Existing robotic climbing strategies tested on vertical surfaces (see text for more details and references).

$$I_{\text{mass}} = \frac{1}{m_{\text{sys}}} \sum_{i=1}^{n_{\text{m}}} m_{\text{ind}} \tag{4.1}$$

where I_{mass} is the mass integration metric, m_{sys} is the system's total mass, n_{m} is the total number of independent modes, and m_{ind} is the required system mass for individual modes. A perfectly integrated system operating in n_{m} independent modes would have a mass integration metric equal to n_{m}, while a value of 1 means no integration.

A mass integration metric is calculated for the S-MAD (330 grams), by considering flight and aerial climbing as two decoupled modes, and perching as a subcomponent of aerial climbing. Specifically, perching and climbing components (i.e., 23 grams for the landing gear and sensor) are considered as unnecessary in flight. For climbing, the wall detection sensor placed on top of the fuselage (i.e., TeraRanger One in Fig. 4.6) and the half of the wing that is not in the propeller slip-stream are considered as unused (i.e., 34 grams). A mass integration metric of 1.83 is obtained, meaning that the average 'dead mass' in the system is just about 8.5% per mode. Comparatively, an I_{mass} of 1.69 was calculated for

the highly-integrated multimodal platform presented in [43], which performs both jumping and gliding.

4.3.2 Vertical climbing energetics

In the past, specific resistance (ε) has been used to compare the horizontal motion energetics of various types of vehicles [42]. Certain studies have also recently used this metric to characterize the efficiency of robotic climbers [24, 35]. Precisely, specific resistance quantifies a system's efficiency in transporting its weight,

$$\varepsilon \triangleq \frac{E}{mgd} = \frac{P}{mgv} \tag{4.2}$$

where m is the system's mass, g is gravitational acceleration, d is the distance traveled, v is the travel speed, E is the energy required to travel distance d, and P is the power required to travel at speed v. The minimum attainable value in vertical climbing is one, if the energy necessary to climb a distance d is exactly equal to the increase in the potential energy of the system (mgd). Using this metric, a performance map was assembled for existing robots and animals (Fig. 4.3).

The resulting map offers interesting insight for system design considerations, by showing clear groups depending on locomotion type. We observe that these trends notably result from a constant power density among robots using comparable climbing strategies. Among existing legged climbers, both robotic and animal [6, 9], an average power density of 25 W/kg is observed. Assuming no losses, this average value would correspond to a maximum theoretical climb speed of 2.5 m/s. In practice, this maximum speed is reduced depending on climbing gait and actuator efficiency. Legged quasi-static (LQS) climbers for example appear largely inefficient when compared to legged dynamic (LD) climbers, which take advantage of body dynamics to optimize their power usage. Data on LD robots however comes mostly from climbing on carpet-covered walls. Dynamical vertical climbing on real-world surfaces has so far only been demonstrated with the BOB platform [24]. A challenge in the design of such systems comes from the need to ensure reliable adhesive attachment during short period of time, which was addressed by integrating compliance through rubber-like materials. Specifically, compliance increases reliability by reducing contact force, but it also reduces speed through material damping, and overall climb efficiency therefore decreases.

Aerial platforms can achieve higher climb speeds because they do not need to interact with the surface until perching, and they generally pack a much higher power density

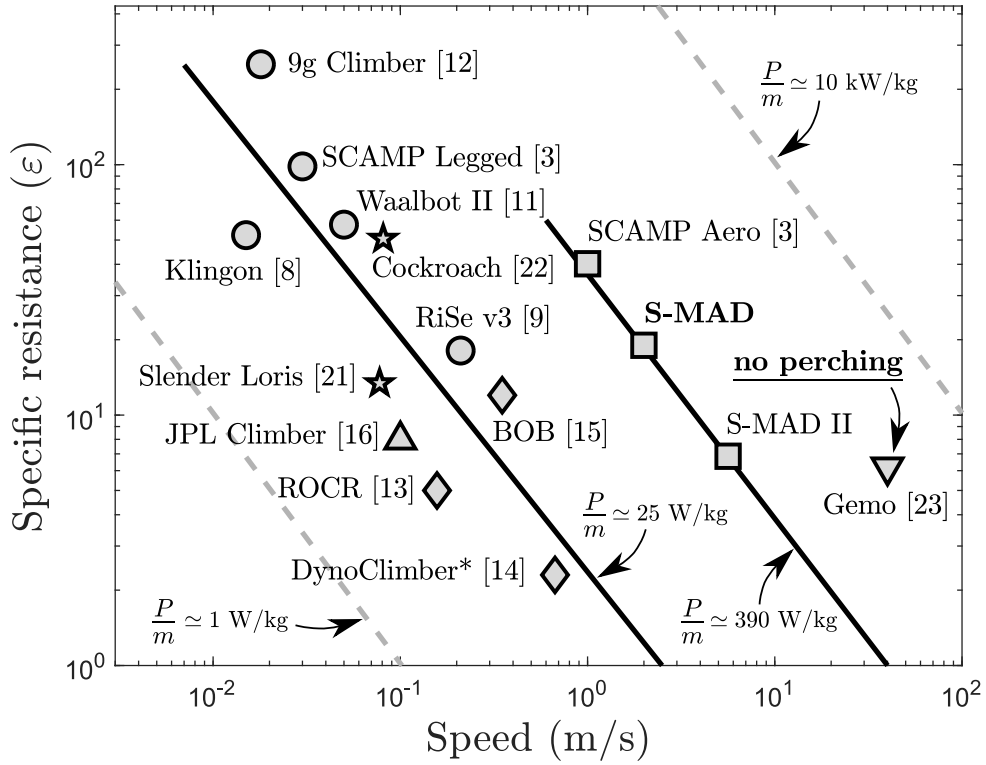

Figure 4.3 Map of ε as a function of speed, for animal species (stars) and robotic platforms : legged quasi-static (circles), legged dynamic (diamonds), wheeled (upward-pointing triangles), multimodal aerial (squares), and regular aerial (downward-pointing triangles). For all data points other than S-MAD, specific resistance was directly obtained from data available in the corresponding published articles. DynoClimber's ε is exceptionnally based on the mechanical power output of its motors, as electrical power input data is not available. S-MAD's specific resistance corresponds to purely vertical climbing (i.e., *rotorcraft mode*), and was obtained through experiment. S-MAD II is a theoretical, improved version of S-MAD, and is detailed in Section 4.6.

(390 W/kg) dedicated almost exclusively to forward thrust. Theoretically, such a power density could allow a maximum vertical speed of 40 m/s. However, the practical speeds attained are much lower, mainly due to aerodynamic losses like drag. Propulsion losses and aerodynamic performance of perching components have also not typically been considered when designing multimodal aerial robots, which can lead to elevated drag and reduced efficiency. Indeed, an RC quadrotor strictly dedicated to flight, such as the Gemo-Copter (P/m = 2438 W/kg) [4], has a specific resistance of only 6.85 and flies upward at an impressive speed of 40 m/s.

Overall, aerial robots are inherently faster climbers than legged robots, due to their higher power density. However, efficient aerial climbing is possible on short distances only if transitions from perching to flight, or transient phases, are executed at a low energetic cost. Such low cost transitions are possible with the S-MAD due to a favorable orientation when perched. This feature leads to a lower specific resistance than most LQS robots, even for a short 5 m climb (Section 4.4). As detailed further, optimizing aerodynamics and propulsion could even allow the system's specific resistance to be reduced by more than 50% (Fig. 4.3 - S-MAD II).

For the current S-MAD system, energetic cost can be reduced in long climbs by taking advantage of the wing to produce lift (i.e., *fixed-wing mode*). Efficient thrust control in vertical flight (i.e., *rotorcraft mode*) can also minimize the specific resistance. The following section therefore discusses the selection of a precise aerial climbing approach and how thrust should be controlled.

4.4 Aerial climbing analysis

Aerial climbing with a fixed-wing UAV can be accomplished in many different configurations, ranging from a near-horizontal climb angle to purely vertical flight. To determine which configuration is best for the S-MAD, climb efficiency as a function of velocity is quantified for different climb angles. Then, the optimal thrust distribution is determined for the selected configuration (vertical flight).

4.4.1 Climbing with thrust and lift

S-MAD's overall climb maneuver is divided in four steps : (1) takeoff to quasi-hover flight, (2) transition maneuver from quasi-hover to climbing, (3) steady climb at a specified angle and speed, (4) perching/landing maneuver. The energetic cost of the first and last steps (takeoff and landing) is practically independent of the climb configuration (speed and

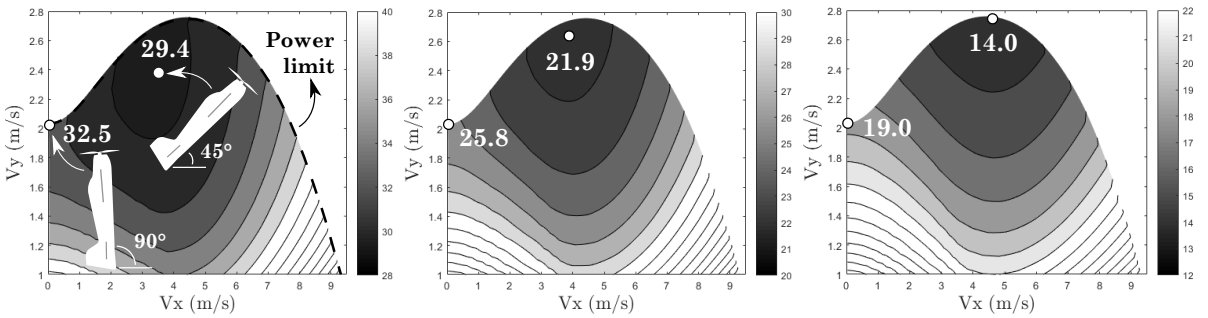

(a) ε with $d = 5$ m (b) ε with $d = 10$ m (c) ε with $d = \infty$

Figure 4.4 Specific resistance as a function of velocity, for different climb heights. Data points are identified for vertical and optimal configuration flight (minimum ε), with corresponding pitch angles (climb angle plus angle-of-attack) shown in (a).

angle) because the duration of those phases in near hover remains almost constant, as observed in simulations and experiments.

Power consumption in transition and in steady climb could however vary significantly with the chosen speed and climb angle. Precisely, non-vertical climb angles enable lift production with the airplane's wing, reducing the energetic cost of climbing. To determine the best climb trajectories, a 3D aerodynamic simulator is used (Khan et al. [14]). This model captures various important aspects of small fixed-wing UAV flight, such as unsteady and high-alpha aerodynamics, effects of control surface deflections, and effects of propeller slipstream. A variable parasitic drag term is notably implemented, to account for a significant variation at low Reynolds number. The non-dimensional thrust coefficient distribution of the propeller is also adjusted until the predicted thrust corresponds to experimental static thrust results (Section 4.6). Simple fixed setpoint PD controllers on elevator and thrust are added to transition from quasi-hover to the desired climb configuration (i.e., climb angle and speed). The simulated thrust and speed, along with motor efficiency, then allow to quantify the energy required to execute the transition maneuver ($E_{\text{transition}}$), and the power consumption while flying at a precise climb configuration (Eq. 4.4). Assuming the airplane eventually performs a maneuver to re-orientate itself towards the wall, and neglecting the energy required to do this, the total energy necessary to execute a climb maneuver is obtained,

$$E = E_{\text{takeoff}} + E_{\text{transition}} + E_{\text{climb}} + E_{\text{perch}} \tag{4.3}$$

where E is the total electrical energy required to execute the maneuver. The constant values determined experimentally for E_{takeoff} and E_{perch} are respectively 12 J and 80 J.

Using Eqs. 4.2 and 4.3, maps of specific resistance as a function of velocity are generated for different climb heights (5 m, 10 m, and ∞) and shown in Fig. 4.4. These maps indicate that for strictly vertical flight that climbing as fast as possible always minimizes energy consumption. Also, it can be observed that minimum specific resistance decreases with height, which is caused by a reduced overall importance in energy consumption for the takeoff, transition and perch phases. The system is therefore more efficient during longer periods of upward flight. It also becomes more efficient to fly with a horizontal velocity during long climbs, as the optimal velocity angle goes down from 90° to 30°, when takeoff, transition and perch energies become negligible (Fig. 4.4c). For climbs shorter than 10 m, vertical flight has a specific resistance only 15% higher than the minimum attainable value. This difference between vertical flight and forward flight would be larger for a platform with better aerodynamic characteristics than the S-MAD (e.g., lower parasitic drag, higher aspect ratio)

Given the relatively small efficiency gain of forward flight for climbs below 10 m, and considering the trajectory generation and tracking that it implies, a choice is made for the remainder of this paper to rely strictly on thrust to climb vertically. Thus, the next section details the usage of a simple model to determine the optimal thrust distribution for vertical aerial climbing.

4.4.2 Climbing with propeller thrust

The optimal thrust distribution for a vertical climb is determined here with a simple 1D physics-based model. To represent S-MAD's propeller, the model uses momentum theory [17], which assumes 1D incompressible airflow, and uniform flow properties in the propeller's disk plane. This theory leads to an analytical equation for mechanical power consumption. This equation depends directly on system parameters and climb speed,

$$P_{\text{mech}} = \kappa T \left(\frac{V_c}{2} + \sqrt{\frac{4(\rho A V_c)^2 + T^2}{2T\rho A}} \right) \tag{4.4}$$

where P_{mech} is the mechanical power required to produce thrust T at climb speed V_c (positive in upward direction), κ is a loss factor determined experimentally (Section 4.6), A is propeller disk area, and ρ is air density.

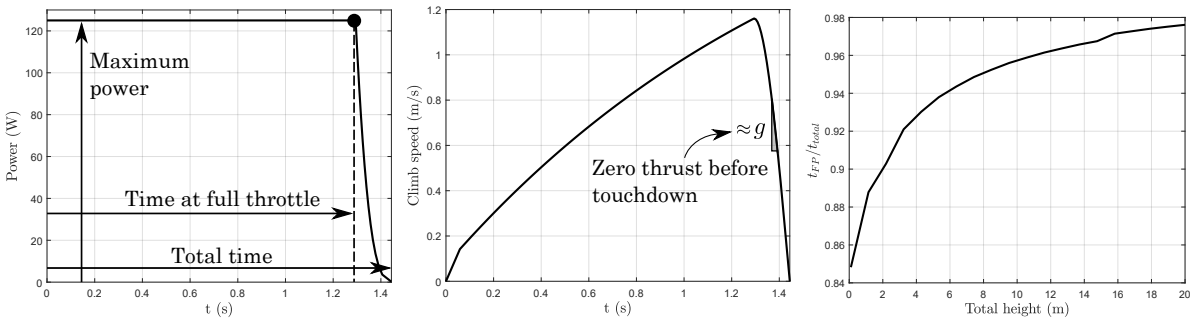

(a) ε with $d = 5$ m (b) ε with $d = 10$ m (c) ε with $d = \infty$

Figure 4.5 Distributions of (a) power and (b) climb speed for a 1 m climb. (c) Ratio of time at full throttle (t_{FT}) to total climb time (t_{total}), as a function of total height - t_{FT} taken when throttle descends below 95% of maximum.

The required thrust to obtain a desired vertical acceleration $\ddot{y}$ during aerial climbing is obtained with the system's equation of motion along the vertical axis (Eq. 4.5),

$$T = \frac{1}{\eta_{\text{effective}}}[m(\ddot{y} + g) + D] \tag{4.5}$$

where m is mass, and g is gravitational acceleration. D is the drag force a drag term including (1) parasitic drag ($C_{D,0} = 0.05$) from the wing, fuselage, and tail, (2) form drag ($C_D = 1.98$) from components in the propeller's wake. Scrubbing drag [36] is represented by a thrust efficiency term ($\eta_{\text{effective}} = 0.83$). The vertical acceleration is obtained through an optimizer, which varies the climb speed distribution to minimize energy consumption over the whole mission, given a precise height to climb and a constraint on available power, as described below :

$$\begin{aligned} \underset{v}{\text{minimize}} \quad & E \\ \text{subject to} \quad & P_{\text{mech}}/\eta_{\text{motor}} \leq P_{\max}, x_{\text{climb}}, \text{Eq.4.5} \end{aligned} \tag{4.6}$$

where E is energy consumption over the whole climb, v is climb velocity, η_{motor} is motor efficiency, $P_{\max}$ is available power, and x_{climb} is the desired climb height.

As shown in Fig. 4.5a, energy consumption for a 1 meter climb is minimized by running the motor at maximum available power, as long as possible, to maximize vertical velocity. A ballistic trajectory is then used to finish the climb (Fig. 4.5b), as the motor is turned off towards the end of the maneuver. The ratio of climbed height at full throttle to total height is shown in Fig. 4.5c. The curve indicates that even for a 2 m climb, more than 90% of the total height should be traveled at maximum available power. This result implies that

an efficient climb maneuver can be implemented with a simple on-off time-based motor control strategy.

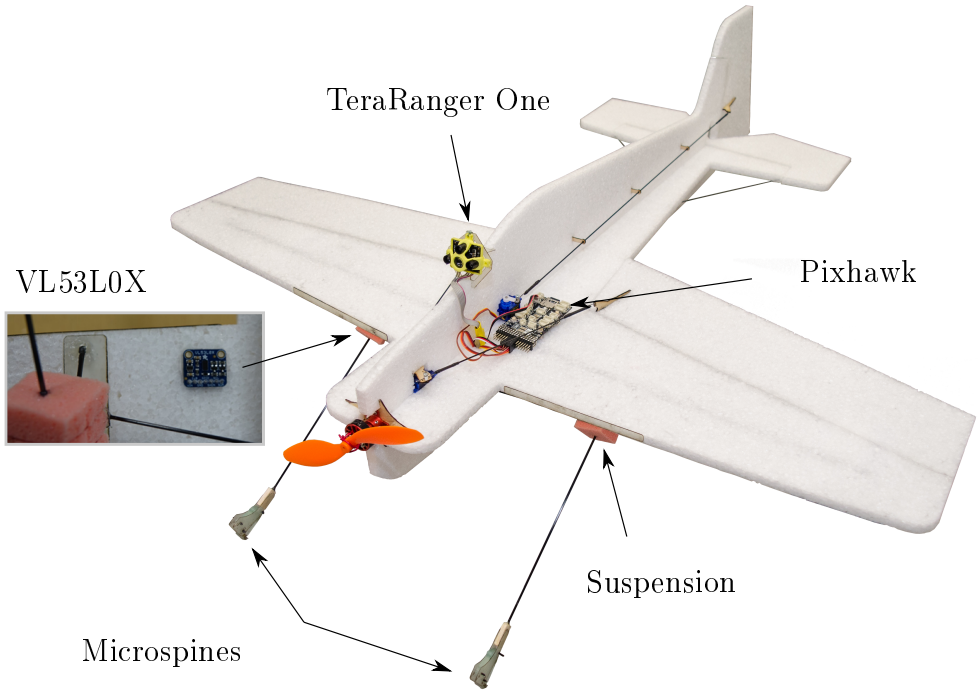

Figure 4.6 S-MAD system overview.

4.5 Aerial climbing implementation

Efficient thrust control can be easily implemented, as presented in the previous section. However, a safe distance from the wall must also be maintained during prolonged climbs, in order to avoid drifting away or flying into the surface. This section details the integrated hardware necessary to perform such wall distance tracking. A simple model and controller design approach are also detailed.

4.5.1 S-MAD platform

In the current S-MAD system (Fig. 4.6), a range sensor is placed under the wing to allow long, controlled vertical climbs in proximity of walls (Adafruit VL53L0X - 1 gram, 10 Hz acquisition frequency, 3-60 cm range). This sensor measures a distance perpendicular to the wing, and is therefore used in conjunction with IMU data to determine wall distance (Fig. 4.8b). Using these sensor measurements, a controller commands elevator deflections to track a desired distance (Fig. 4.7). This ensures that the robot climbs without drifting away from the surface, staying in sensor range, while other decoupled controllers track

constant yaw and roll orientation commands, through ailerons and rudder deflections [8] (Fig. 4.7).

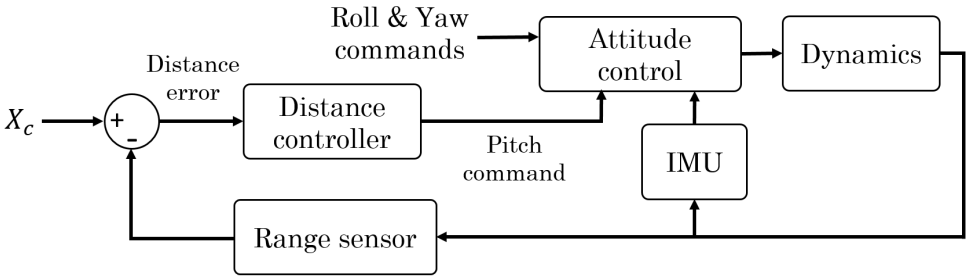

Figure 4.7 Block diagram of the wall distance controller.

Although the range sensor is mainly used in this climbing controller, it also brings advantages during the final stages of the perching maneuver. Indeed, the system previously relied on accelerometer readings to detect wall impacts. This method was however subject to false detections in the presence of perturbations (e.g., wind gust) and variable sensing delays. Preemptive wall impact detection, through VL53L0X sensor, enables more reliable outdoor perching, but also allows the integration of a larger propeller, because of a reduced risk of having the propeller collide with walls. This leads directly to more efficient vertical climbing, as a lower propeller disk loading results in reduced power consumption [17].

The control of this propulsion system is performed through constant or time-dependent commands :

1. **Takeoff and climb :** the maximum thrust command (about $1.5mg$) is sent for a duration that is function of the height to be climbed, as full throttle maximizes efficiency (Section 4.4).
2. **Slow down and landing :** a constant thrust command slightly lower than mg is sent for 0.5 s. This adds robustness by ensuring that the system does not fall too fast downward if the microspines are not immediately inserted into asperities at touchdown.
3. **Relaxation :** a ramp-down command, from a 65% thrust to 0%, allows the airplane to settle down at its new position and avoid propeller contact with the surface, while engaging micropsines.

4.5.2 Low-fidelity model for climbing stability analysis

The feasibility of distance tracking in climb with the S-MAD is initially verified with a simple model (Fig. 4.8a) and a root locus analysis. The model considers only horizontal

and pitch motion of the system, where the elevator deflection is the control input and the horizontal position is the output. The airplane's orientation remains mostly vertical, allowing a small angle approximation on θ and constant vertical speed assumption.

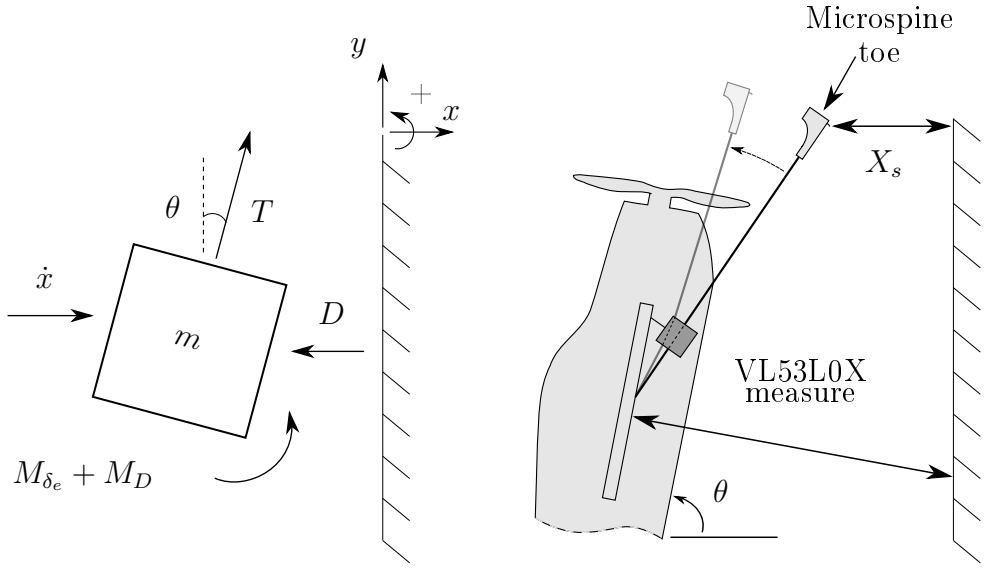

Figure 4.8 (a) Free body diagram of climbing, and (b) schematic of S-MAD's suspension, where X_s is the minimum safe horizontal distance between the microspines and the wall.

The horizontal drag (D) would usually be represented as $1/2\rho A C_D \dot{x}^2 sign(\dot{x})$. As the sign of the nonlinear horizontal drag force acting on the fuselage and wing (Eq. 4.7) changes with the direction of horizontal velocity, the following linearisation is used :

$$D = c\dot{x} \tag{4.7}$$

where c is the linearization coefficient, and $\dot{x}$ is horizontal velocity. A representative velocity range of ± 0.3 m/s was selected through experiments for best fit.

The moment M_{δ_e} produced on the body by an elevator deflection can be expressed with Eq. 4.8,

$$M_{\delta_e} = \frac{1}{2}\rho V^2 C_{Le} A_e d_{CM} = M\delta_e \tag{4.8}$$

where V is the total velocity (assumed to be constant) of the airflow passing over the elevator (climb velocity and propeller-induced flow velocity), A_e is the elevator area, and d_{CM} is the moment arm (distance from elevator to center of mass). The term C_{Le} is the

elevator lift coefficient, defined with a linearized equation,

$$C_{Le} = C_{Le,\delta_e}\delta_e \tag{4.9}$$

where C_{Le,δ_e} is the lift increment with control surface deflection, and δ_e is the elevator deflection angle. The C_{Le,δ_e} value is taken from [27], for a rectangular area with $AR = 3$. This expression for the elevator lift coefficient is reasonable given small variations of θ, and a vertical flow velocity signficantly higher than angular and lateral motion velocity. The downward drag caused by elevator deflections remains negligible as other, more signficant vertical drag losses are taken into account by considering a constant upward velocity. Similarly, the moment from horizontal drag on the elevator, at lateral velocity, remains signficantly smaller than the moment produced with elevator deflections (30 times smaller at maximum elevator deflection).

Using these force definitions and approximations (small θ angle and negligible elevator drag), the equations of motion are,

$$T\theta - D = m\ddot{x} \tag{4.10a}$$

$$M_{\delta_e} + M_D = I\ddot{\theta} \tag{4.10b}$$

where m and I are respectively the system's mass and moment of inertia around CM, $\ddot{x}$ is horizontal acceleration, $\ddot{\theta}$ is angular acceleration, and M_D is angular drag, defined as a linear function of angular speed ($M_D = -b\dot{\theta}$). Applying Laplace transforms to Eq. 4.10, the second-order systems in Eq. 4.11 can be defined,

$$\frac{X(s)}{\theta(s)} = \frac{T}{ms^2 + cs} \tag{4.11a}$$

$$\frac{\theta(s)}{\delta_e(s)} = \frac{M}{Is^2 + bs} \tag{4.11b}$$

The block diagram in Fig. 4.9 shows these Laplace representations of linear and angular motion, and the associated proportional-derivative controllers ($C_1(s)$ and $C_2(s)$).

This representation is then used to define the system as a single transfer function, allowing preliminary controller gain identification through a root locus analysis. Using the controller gains already implemented on the S-MAD for attitude tracking in hover ($C_2(s)$), the

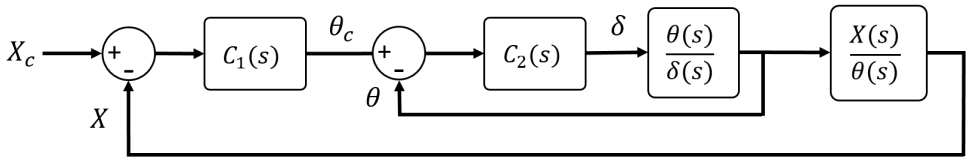

Figure 4.9 Climb control diagram for the 4th-order system.

proportional gain of the distance controller ($K_{p,x}$) can be initially selected by assuming a null derivative gain ($K_{d,x}$). A damping criterion $\zeta = 0.707$ on the two dominant poles can be reached with a value of $K_{p,x} = 0.042$, showing that the desired stability can be achieved without a derivative gain.

This analysis confirms the feasibility of the proposed controller, but also gives insight for the order of magnitude of the necessary controller gains. Indeed, the resulting $K_{p,x}$ is used as a guideline for gain identification with a high-fidelity model. The range of acceptable values for $K_{p,x}$ and $K_{d,x}$ can be refined with this initial approximation, allowing a reduced number of simulations.

4.5.3 High-fidelity model for controller gain identification

The 3D aerodynamic model mentioned in Section 4.4 is used here for precise gain identification. The model includes the delay from the range sensor, but also other delays such as those introduced by servo update rate (50 Hz). It is used to simulate climbs lasting between 1 and 5 seconds, which respectively correspond to climbs between 0.7 m and 7 m. These simulations are performed with different combinations of $K_{p,x}$ and $K_{d,x}$, to determine which controller minimizes the quadratic position error cost function,

$$J = \int_{t_0}^{t_1} {x_e}^2 dt \tag{4.12}$$

where J is cost, and x_e is the horizontal position tracking error. Notably, J includes no weight for actuator commands (servomotor), because of the low power consumption that it represents. Using this cost definition, with $K_{p,x}$ and $K_{d,x}$ values ranging form 0 to 0.1, and a climb lasting 5 seconds, the cost map in Fig. 4.10 is obtained.

The map shows that cost is minimized with a gain combination of $K_{p,x} = 0.055$ and $K_{d,x} = 0.01$. This observation holds regardless of climb time for the range tested, as the transient part of the response is relatively short (below 1 s). Overall, cost is mainly driven by the proportional gain and, for the real system, gains $K_{p,x} = 0.05$ and $K_{d,x} = 0$ are selected. This combination prevents derivation of the distance sensor measurements

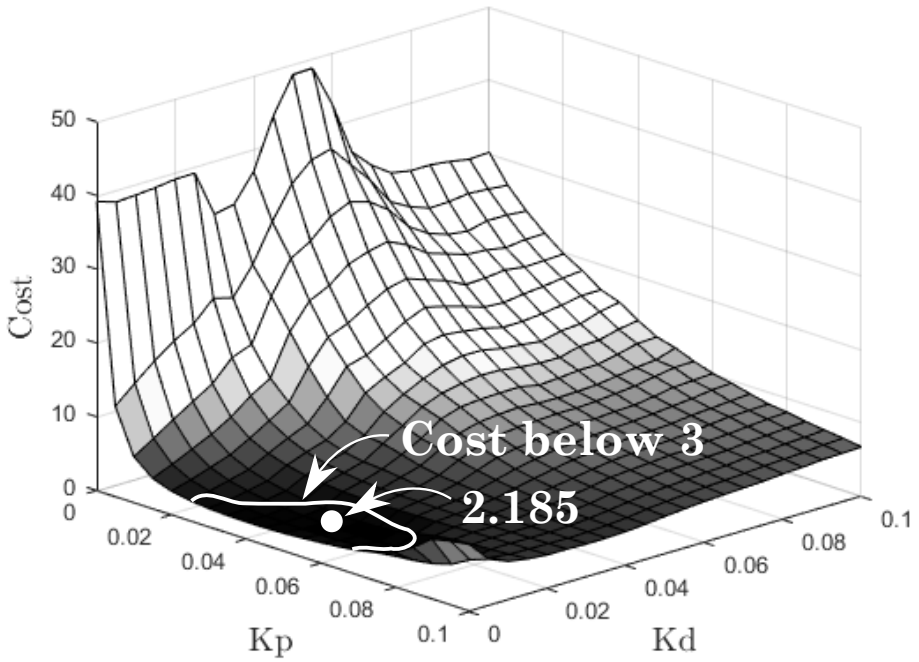

Figure 4.10 Cost as a function of proportional (K_p) and derivative (K_d) gains for distance control, over a 5 second climb. The minimum cost (2.185) is identified, along with the region for which cost remains below 3.

updated at 10 Hz. According to the cost definition, the gains selected show practically optimal performance (10% cost increase).

4.6 Results and Discussion

The controllers presented in Section 4.5 are implemented on the S-MAD, and the climb trajectory is demonstrated. The approach used to calculate power consumption for the propulsion system is also presented, along with possible system ameliorations.

4.6.1 Climbing maneuver validation

The climbing control strategy is implemented on S-MAD's PixHawk microcontroller, and tested indoor. The experimental CM position of the airplane is measured with a motion capture system, and plotted along corresponding simulation data in Fig. 4.11. The trajectories globally agree, confirming the predicted control strategy's performance. Simulation results for other gain values also show the necessity for a well-adjusted controller. For example, if the gain is too small, the airplane remains close to the surface while climbing upward, potentially causing the landing gear to hit the surface at a bad loading angle. A larger gain leads to significant overshoot, potentially moving the airplane out of sensor range.

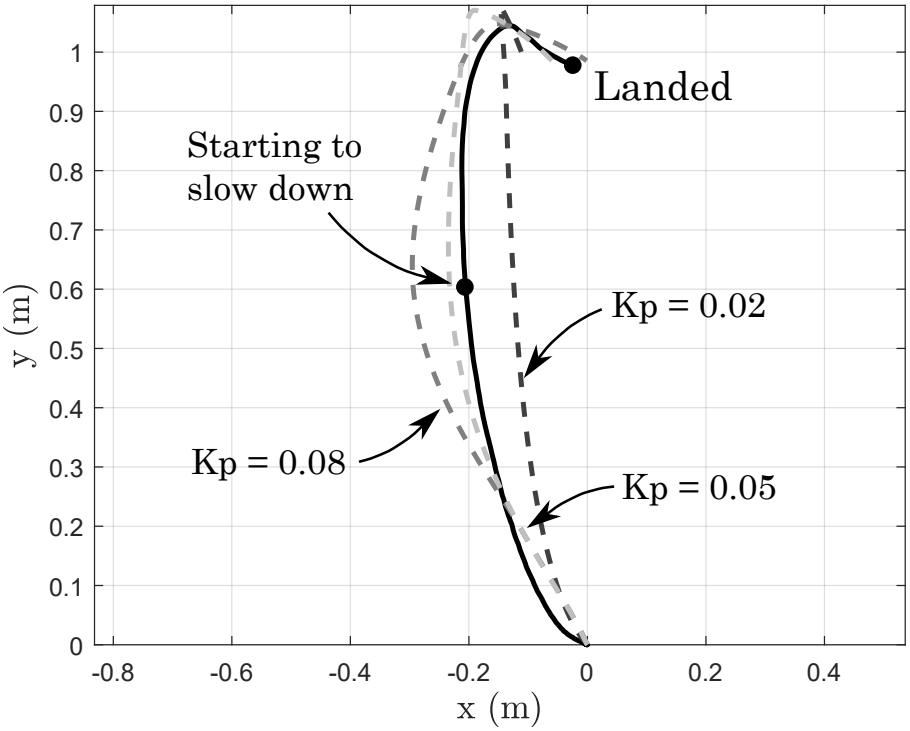

Figure 4.11 Experimental measurements of CM position during a 1 m climb with $K_d = 0.05$ (black), for a desired horizontal position of -0.18 m. Simulations of CM position for different proportional gains are also shown in dashed, with $K_d = 0$.

4.6.2 Model calibration and specific resistance calculation

The specific resistance for the implemented climb maneuver is calculated with a simple model, after experimentally identifying propeller losses. First, the propulsion system's maximum thrust, efficiency, and associated power consumption are quantified with a static thrust test bench ($T = 5.0$ N, $P = 115$ W, $\eta_{\text{motor}} = 47\%$). The data obtained is then used to identify the loss factor κ in Eq. 4.4 ($V_c = 0$). Knowledge of this parameter ($\kappa = 1.55$) and Eq. 4.4 enables a conservative estimation of power consumption for a full throttle climb, by assuming that thrust remains roughly the same as in the static propulsion test ($T = 5.0$ N), and by using the maximum vertical speed measured with a motion capture system ($V_c = 2$ m/s). Power consumption and climb speed values are then used to calculate S-MAD's specific resistance ($\varepsilon = 19$, for $d = \infty$).

4.6.3 Improving climb performance

S-MAD's specific resistance compares favorably with various existing robotic climbers (Fig 4.3). This specific resistance could however be improved with better aerodynamic characteristics, and higher motor efficiency. Notably, the parasitic drag coefficient of RC airplanes can be as low as 0.02 [14], while S-MAD's $C_{D,0}$ was found to be approximately 0.06 at maximum vertical climb speed. The system's propulsion efficiency is also reduced by the current component integration (e.g., loose electric wiring, large motor mount, etc.), which could be improved by adding a light, aerodynamic fuselage (e.g., plastic film). A system re-design could also lead to a better motor-propeller combination, as small brushless DC motors in RC vehicles are able to reach efficiencies above 0.7 [27], while S-MAD's current motor reaches only 0.47 in climb. Considering a fuselage area 50% smaller (less drag), and a conservative motor efficiency of 0.6, the aerodynamic model developed by Khan et al. [14] predicts a specific resistance below 7 for a steady vertical climb.

4.7 Conclusions and Future Work

A new way of climbing vertical surfaces has been demonstrated with the S-MAD, a motorized fixed-wing UAV. The climbing approach is enabled by S-MAD's favorable thrust orientation when perched, and its high thrust-to-weight ratio. The low amount of added mass from perching and sensing components leads to a light and integrated architecture, conserving a high power density while adding versatility. These features allow the system to efficiently and reliably perform fast aerial climbing, while avoiding power losses inherent to legged robots.

Future work will be focused on allowing the system to perch on more varied surfaces (e.g., glass), and perform autonomous missions involving climbing and transitions between different vertical surfaces.

CHAPITRE 5
CONCLUSION

Ce projet a mené à la conception et la fabrication d'un drone percheur à aile fixe. La faible masse de la suspension développée permet à l'avion d'exécuter des atterrissages robustes, sans affecter considérablement ses performances de vol. Entre autres, la faible masse de cette suspension et la poussée aérodynamique élevée du système de propulsion permettent des manoeuvres uniques, comme des manoeuvres de grimpe le long de surfaces verticales. Le fonctionnement des atterrissages, des décollages et des manoeuvres de grimpe a été testé en conditons réelles à de multiples reprises.

En plus du développement d'un prototype physique d'avion percheur, plusieurs modèles ont été développés pour guider la conception des contrôleurs et des composantes nécessaires à la réalisation des différentes phases d'opération de l'avion. Afin de prédire les performances de la suspension intégrée, un modèle d'impact a été développé et validé exprimentalement. Ce modèle a ultimement permis d'identifier l'enveloppe d'atterrissage de l'avion, prédisant en fonction des conditions d'impact si l'avion réussit à se percher. Les résultats du modèle ont ensuite permis, conjointement avec un modèle aérodynamique, d'identifier un gain de contrôleur pour la portion aérienne de la manoeuvre d'atterrissage. En variant différents paramètres du systèmes et conditions initiales pour simuler plusieurs cas, un gain maximisant la robustesse de la manoeuvre d'atterrissage a pu être identifié. Pour la phase de grimpe aérienne le long de surface verticales, deux modèles aérodynamiques ont été développés, afin de (1) déterminer la distribution de poussée aérodynamique optimale et (2) identifier un contrôleur pour le maintien d'une position horizontale. Le deuxième modèle est particulièrement utile, alors qu'il permet d'étudier la stabilité d'un contrôleur en fonction de seulement quelques paramètres système majeurs (surface alaire, poussée, etc.) Enfin, une analyse comparative entre différentes techniques de grimpes a permis d'établir l'intérêt d'utiliser des techniques de montée aériennes. Les observations établies permettront dans le futur de guider le développement de plateformes robotiques multimodales.

À court terme, les étapes futures dans le développement d'un drone percheur multimodal comprendront principalement une re-conception de la plateforme de vol. Notamment, l'intégration de deux moteurs pour la propulsion, au lieu d'un seul, permettrait de rendre la manoeuvre d'atterrissage encore plus robuste, en éliminant les problèmes d'effet gyro-

scopique et de couple de réaction du moteur qui ont été notés. Une meilleure sélection de moteurs et d'hélices permettrait également d'augmenter l'efficacité de l'avion en grimpe. De plus, en éliminant le fuselage de l'avion, d'importants gains pourraient être faits en termes de performances aérodynamiques. Or, à plus long terme, l'intégration d'un système d'adhésion plus robuste serait nécessaire puisque, lorsqu'il est en position perchée, l'avion peut encore se décrocher si des vents latéraux le perturbent. L'utilisation d'un système de griffes opposées permettrait de maintenir sa position, même lors de conditions environnementales plus difficiles. L'ajout d'autres technologies d'adhésions ouvrirait également la porte à une plus grande versatilité. Par exemple, l'intégration d'adhésifs inspirés du Gecko, en plus des microgriffes déjà présentes, permettrait des atterrissages sur des surfaces lisses en plus de surfaces rugueuses. Enfin, des stratégies de rétablissement suite à des atterrissages ratés pourraient éliminer toutes incertitudes sur le système lorsqu'il est en opération.

LISTE DES RÉFÉRENCES

[1] Asbeck, A. et et al. (2006). Scaling hard vertical surfaces with compliant microspine arrays. *The International Journal of Robotics Research*.

[2] Beardsley, P., Siegwart, R., Arigoni, M., Bischoff, M., Fuhrer, S., Krummenacher, D., Mammolo, D. et Simpson, R. (2015). Vertigo-a wall-climbing robot including ground-wall transition. *Disney Research*.

[3] Daler, L. et et al. (2013). A perching mechanism for flying robots using a fibre-based adhesive. Dans *International Conference on Robotics and Automation*.

[4] Dirk Brunner (2018). Extreme high power drone with highest climb rate. `http://www.research-drone.com/en/extreme_climb_rate.html`.

[5] Estrada, M. A., Hawkes, E. W., Christensen, D. L. et Cutkosky, M. R. (2014). Perching and vertical climbing : Design of a multimodal robot. Dans *Robotics and Automation (ICRA), 2014 IEEE International Conference on*, IEEE. p. 4215–4221.

[6] Full, R. J. et Tullis, A. (1990). Energetics of ascent : insects on inclines. *Journal of Experimental Biology*, volume 149, numéro 1, p. 307–317.

[7] Graule, M. et et al. (2016). Perching and takeoff of a robotic insect on overhangs using switchable electrostatic adhesion. *Science*.

[8] Green, W. E. et Oh, P. Y. (2009). A hybrid mav for ingress and egress of urban environments. *IEEE Transactions on Robotics*.

[9] Hanna, J. B. et Schmitt, D. (2011). Locomotor energetics in primates : gait mechanics and their relationship to the energetics of vertical and horizontal locomotion. *American journal of physical anthropology*, volume 145, numéro 1, p. 43–54.

[10] Hawkes, E. W., Christensen, D. L. et Cutkosky, M. R. (2015). Vertical dry adhesive climbing with a 100× bodyweight payload. Dans *Robotics and Automation (ICRA), 2015 IEEE International Conference on*, IEEE. p. 3762–3769.

[11] Haynes, G. C., Khripin, A., Lynch, G., Amory, J., Saunders, A., Rizzi, A. A. et Koditschek, D. E. (2009). Rapid pole climbing with a quadrupedal robot. Dans *Robotics and Automation, 2009. ICRA'09. IEEE International Conference on*, IEEE. p. 2767–2772.

[12] Howell, L. L. (2001). *Compliant mechanisms*. John Wiley & Sons.

[13] Kalantari, A. et et al. (2015). Autonomous perching and take-off on vertical walls for a quadrotor micro air vehicle. Dans *Int. Conf. on Robotics and Automation*.

[14] Khan, W. et Nahon, M. (2016). Modeling dynamics of agile fixed-wing uavs for real-time applications. Dans *International Conference on Unmanned Aircraft Systems*.

[15] Kim, S., Spenko, M., Trujillo, S., Heyneman, B., Mattoli, V. et Cutkosky, M. R. (2007). Whole body adhesion : hierarchical, directional and distributed control of adhesive forces for a climbing robot. Dans *Robotics and Automation, 2007 IEEE International Conference on*, IEEE. p. 1268–1273.

[16] Kovač, M., Germann, J., Hürzeler, C., Siegwart, R. Y. et Floreano, D. (2009). A perching mechanism for micro aerial vehicles. *Journal of Micro-Nano Mechatronics*.

[17] Leishman, G. J. (2006). *Principles of helicopter aerodynamics with CD extra*. Cambridge university press.

[18] Liu, Y., Sun, G. et Chen, H. (2014). Impedance control of a bio-inspired flying and adhesion robot. Dans *International Conference on Robotics and Automation*.

[19] Lussier Desbiens, A. (2012). *Landing and Perching on Vertical Surfaces*. Thèse de doctorat, Stanford University.

[20] Lussier Desbiens, A., Asbeck, A. T. et Cutkosky, M. R. (2011). Landing, perching and taking off from vertical surfaces. *The International Journal of Robotics Research*.

[21] Lynch, G. A., Clark, J. E., Lin, P.-C. et Koditschek, D. E. (2012). A bioinspired dynamical vertical climbing robot. *The International Journal of Robotics Research*, volume 31, numéro 8, p. 974–996.

[22] Mehanovic, D., Bass, J., Courteau, T., Rancourt, D. et Desbiens, A. L. (2017). Autonomous thrust-assisted perching of a fixed-wing uav on vertical surfaces. Dans *Conference on Biomimetic and Biohybrid Systems*, Springer. p. 302–314.

[23] Mehanovic, D., Rancourt, D. et Desbiens, A. L. (2019). Fast and efficient robotic climbing. Dans *IEEE Robotics and Automation Letters*, IEEE.

[24] Miller, B. D., Rivera, P. R., Dickson, J. D. et Clark, J. E. (2015). Running up a wall : the role and challenges of dynamic climbing in enhancing multi-modal legged systems. *Bioinspiration & biomimetics*, volume 10, numéro 2, p. 025005.

[25] Mitiguy, P. (????). Advanced dynamics and motion simulation.

[26] Moore, J., Cory, R. et Tedrake, R. (2014). Robust post-stall perching with a simple fixed-wing glider using lqr-trees. *Bioinspiration & biomimetics*.

[27] Mueller, T. J., Shkarayev, S. V. et Ifju, P. (2000). *Introduction to the design of fixed-wing micro air vehicles : including three case studies*. American Institute of Aeronautics and Astronautics.

[28] Murphy, M. P., Kute, C., Mengüç, Y. et Sitti, M. (2011). Waalbot ii : Adhesion recovery and improved performance of a climbing robot using fibrillar adhesives. *The International Journal of Robotics Research*, volume 30, numéro 1, p. 118–133.

[29] Myeong, W. et et al. (2015). Development of a drone-type wall-sticking and climbing robot. Dans *Int. Conf. on Ubiquitous Robots and Ambient Intelligence*.

[30] Nie, C., Corcho, X. P. et Spenko, M. (2013). Robots on the move : Versatility and complexity in mobile robot locomotion. *IEEE Robotics & Automation Magazine*, volume 20, numéro 4, p. 72–82.

[31] Noth, A. (2008). *Design of Solar Powered Airplanes for Continous Flight*. Thèse de doctorat, ETH Zurich.

[32] Parness, A., Soto, D., Esparza, N., Gravish, N., Wilkinson, M., Autumn, K. et Cutkosky, M. (2009). A microfabricated wedge-shaped adhesive array displaying gecko-like dynamic adhesion, directionality and long lifetime. *Journal of the Royal Society Interface*, p. rsif–2009.

[33] Pope, M. T., Kimes, C. W., Jiang, H., Hawkes, E. W., Estrada, M. A., Kerst, C. F., Roderick, W. R., Han, A. K., Christensen, D. L. et Cutkosky, M. R. (2017). A multimodal robot for perching and climbing on vertical outdoor surfaces. *IEEE Transactions on Robotics*, volume 33, numéro 1, p. 38–48.

[34] Prahlad, H., Pelrine, R., Stanford, S., Marlow, J. et Kornbluh, R. (2008). Electroadhesive robots—wall climbing robots enabled by a novel, robust, and electrically controllable adhesion technology. Dans *Robotics and Automation, 2008. ICRA 2008. IEEE International Conference on*, IEEE. p. 3028–3033.

[35] Provancher, W. R., Jensen-Segal, S. I. et Fehlberg, M. A. (2011). Rocr : An energy-efficient dynamic wall-climbing robot. *IEEE/ASME Transactions on Mechatronics*, volume 16, numéro 5, p. 897–906.

[36] Raymer, D. P. (2006). *Aircraft Design : A Conceptual Approach (AIAA Education)*. Virginia : American Institute of Aeronautics & Astronautics.

[37] Ritz, R. et D'Andrea, R. (2017). A global controller for flying wing tailsitter vehicles. Dans *Robotics and Automation (ICRA), 2017 IEEE International Conference on*, IEEE. p. 2731–2738.

[38] Roderick, W. R., Cutkosky, M. R. et Lentink, D. (2017). Touchdown to take-off : at the interface of flight and surface locomotion. *Interface Focus*.

[39] Ruffatto, Donald (2018). personal communication.

[40] Schmidt, D. et Berns, K. (2013). Climbing robots for maintenance and inspections of vertical structures—a survey of design aspects and technologies. *Robotics and Autonomous Systems*, volume 61, numéro 12, p. 1288–1305.

[41] Thomas, J. et et al. (2016). Aggressive flight with quadrotors for perching on inclined surfaces. *Journal of Mechanisms and Robotics*.

[42] Von Karman, T. et Gabrielli, G. (1950). What price speed ? specific power required for propulsion of vehicles. *Mechanical Engineering*, volume 72, p. 775–781.

[43] Woodward, M. A. et Sitti, M. (2014). Multimo-bat : a biologically inspired integrated jumping–gliding robot. *The International Journal of Robotics Research*, volume 33, numéro 12, p. 1511–1529.